

X-ray Emission Line Profiles from the Magnetically Confined Wind Shock Model

Swarthmore College Senior Thesis in Astrophysics

*Swarthmore College Department of Physics and Astronomy,
500 College Ave., Swarthmore PA 19081*

Stephanie Tonnesen

advisor: Professor David H. Cohen

ABSTRACT

O stars make important contributions to the energy and composition of the interstellar medium through their stellar winds and tendency to become supernovae. The *Chandra* satellite has recently observed X-ray emission lines from these stellar winds, producing spectra of unprecedented resolution. One of these observed stars is the young star θ^1 Orionis C. The X-ray lines from this star are narrow and symmetric, in direct contrast to the line profiles observed from ζ Puppis, which has a standard X-ray emitting wind. In addition, observations of Zeeman splitting and optical polarization have detected a magnetic field around this star (Donati et al., 2002). θ^1 Orionis C is unusual in that its rotational axis is misaligned from both the magnetic field axis and the observer’s axis. This allows us to view this star from all possible angles with respect to the magnetic axis. In order to examine the wind structure producing the narrow, symmetric X-ray emission line profiles from θ^1 Orionis C, we calculate analytic and numerical models based on an adaptation of the Magnetically Confined Wind Shock (MCWS) model. From these models we are able to create line profiles that can be compared to observed line profiles from θ^1 Orionis C. Here we describe the process by which our program creates line profiles from analytic and numerical wind models. We find that our most sophisticated model, a numerical magnetohydrodynamic (MHD) simulation of a non-isothermal wind that emits X-rays from material with a temperature over 10^6 K, matches the data well. The characteristics of the line profiles from the model and the data are consistent in three important ways: the lines are narrow; the centroids of the line profiles do not shift far from the rest wavelength; and the flux decreases with increasing viewing angle. We conclude that our adaptation of the MCWS model is a good description of the wind structure around θ^1 Orionis C, and around other hot stars with magnetic fields.

1. Introduction

1.1. Introduction to O type stars

O type stars are the hottest stars. Because there are few hot stars in a galaxy, they contribute little to its total mass. However, these stars are so luminous that they contribute a disproportionate amount to the total light of the galaxy. In fact, their luminosity is so great that the force of their radiation drives some of their material into the interstellar

medium. Because of their stellar winds and their ability to become supernovae, these stars input energy and material into the interstellar medium. They are vital to the evolution of the stellar population because they fuse their own material into more metal-rich gas that will create and fuel the next generation of stars.

O stars have effective (surface) temperatures that are greater than 34000 K, at least six times the solar temperature. These stars are incredibly massive, with masses of up to $120 M_{\odot}$. Luminosity in a blackbody is proportional to temperature raised to the fourth power. This relationship shows that the luminosities of O stars will be many orders of magnitude larger than those of solar type stars. Because their luminosity is up to 10^6 times the luminosity of the sun they contribute much of the luminosity of the galaxy (Lamers & Cassinelli, 1979), even though there are fewer of them than there are solar type G stars.

Unlike in the Sun, luminosity is the driving force behind O stars' stellar winds. In a solar-type star, the high temperature and density in the corona cause high pressure that drives the material away from the star in a wind. However, O stars have no corona; thus, they do not have enough gas pressure to drive their mass loss. Instead, these stars have radiation-driven winds. Photons leave the star with some momentum $p = \frac{h\nu}{c}$ that is then imparted to an atom when line scattering occurs. Line scattering occurs when a photon excites an atom, and then a photon of the same energy is immediately emitted when the atom de-excites. Although an atom in the wind emits photons isotropically, all the photons the atom absorbs have an outward momentum from the star, imparting a net outward momentum to the gas. Because the luminosity of hot stars is high, there is a large number of scattering events, and thus the amount of material the star continuously loses is also high. An average mass loss rate for an O star is 10^{-6} solar masses per year, whereas the average mass-loss rate for the sun is about $10^{-14} M_{\odot}\text{yr}^{-1}$ (Lamers & Cassinelli, 1979). A $20 M_{\odot}$ star has a main-sequence lifetime of about 10^7 years (Ostlie & Carroll, 1996), which means that in its lifetime it drives 10 solar masses of material into the interstellar medium. The wind is very dense because so much material is being ejected from the star. In a star with a stationary spherically symmetric wind, the mass continuity equation describes the flow of mass through the area around the star and can be solved for the wind density as a function of radius.

$$\rho(r) = \frac{\dot{M}}{4\pi r^2 v(r)} \quad (1)$$

\dot{M} is the constant mass-loss rate, r is the radial distance from the center of the star, and $v(r)$ is the velocity at some radius. For an O5 star like θ^1 Orionis C with a mass loss rate of 10^{-6} solar masses per year, a terminal velocity of 2500 km s^{-1} , and a radius of $15 R_{\odot}$, we find the typical wind density to be about 10^{10} cm^{-3} .

Hot stars must use radiation to drive their stellar winds, rather than gas pressure,

because they lack magnetic fields. The strong magnetic fields in the sun result from the movement of charge through convection. There is no convection in a hot star, so there is no magnetic dynamo to generate a corona. Because hot stars cannot have the same type of magnetic fields as cool stars and the mechanism by which a magnetic field might occur on a hot star is unknown, astronomers believed that hot stars did not have any magnetic fields. With the use of optical polarization observations and evidence of Zeeman splitting, however, some O and B stars have been found to have magnetic fields. Specifically, spectropolarimetric observations have revealed a dipole field around θ^1 Orionis C (an O7 V star (Gagne et al., 1997)). At about 200,000 years old, this is a young star even in terms of O star main sequence lifetimes, which are on the order of 10^6 years, so its magnetic field may be a primordial field that was created at the star's birth (Donati et al., 2002).

1.2. X-ray Discovery

Observers using the *Einstein* X-ray satellite discovered that hot stars are strong X-ray emitters (Harnden et al., 1979; Seward et al., 1979). One theory explaining this phenomenon is that the X-rays come from the surface of the star in coronal emission (Cassinelli & Olson, 1979). However, many studies have limited the extent, temperature, and fractional X-ray output of such a corona to the extent that this theory is unlikely (Cassinelli, Olson & Stalio, 1978; Nordsieck, Cassinelli & Anderson, 1981; Cassinelli & Swank, 1983; Baade & Lucy, 1987; MacFarlane et al., 1993). In addition, as described in the previous subsection, there is no theoretical expectation for O stars to have coronae. A more likely theory is that the X-rays are being emitted by the stellar wind. This means that there is some mechanism in the wind that is heating the material up to temperatures in excess of 10^6 K, hot enough to emit high-energy X-ray photons (Lamers & Cassinelli, 1999). One plausible model is the standard wind shock model, which uses the inherent instabilities in the wind as the means by which the wind is shock heated to a temperature at which it emits X-rays. These instabilities are a direct result of the physics of Doppler deshadowing and line driving in winds (Owocki, Castor, & Rybicki 1988). This model is of a spherically symmetric wind whose inherent instabilities cause some of the material to be moving faster or slower than the average flow. These instabilities are propagated until fast-moving material collides with slower material and causes a shock. There is an equation relating the temperature of the shocked material to the velocity of the shock.

$$T_{shock} \propto v_{shock}^2 \quad (2)$$

The wind instability model fits the observational data of ζ Pup, which is an older O star with no observed magnetic field. The X-rays from this star are soft and the spectrum consists of broad, asymmetric lines (Hillier et al., 1993; Kramer, Cohen, & Owocki, submitted 2003).

Unfortunately, the instability model cannot explain the hardness of the X-rays in the wind of θ^1 Orionis C (Schulz et al., 2000) as the shock velocity is not large enough to cause the high temperatures necessary to excite the wind material into radiatively emitting hard X-rays.

1.3. The Magnetically Confined Wind Shock Model

A model has been introduced that includes the dipole magnetic fields discovered on θ^1 Orionis C (Donati et al, 2002). These fields can channel the wind from the poles toward the equator along the field lines (Babel & Montmerle, 1997; ud-Doula & Owocki, 2002), creating shocks along the equator that are strong enough to produce hard X-rays. This dynamic interplay between the magnetic field and the wind outflow is the Magnetically Confined Wind Shock model (MCWS).

This model can simulate data that would be observed from a star with this wind structure. We now have the ability to obtain data with enough detail to allow fruitful comparison because of new instrumentation. The *Chandra* satellite has spectroscopic resolution capability that is better than the *Einstein* satellite by over two orders of magnitude¹. This high resolution allows us to use the line profiles to understand the kinematics and structures in the winds. We are motivated to create line profiles from the simulations by two main factors: using *Chandra*, we are able to obtain line profiles with more detail than ever before; and we have, for the first time, detailed computer simulations of MCWS models.

Our research bridges the gap between the theoretical MCWS model and observational data from θ^1 Orionis C, a star with hard X-ray emission and an observed dipole magnetic field. We adapted the MCWS paradigm to create both analytic models and magnetohydrodynamic simulations (ud-Doula, 2002) of the wind around a hot star with a dipole magnetic field. Our analytic models produce simplified, steady-state velocity and density profiles of a structured wind, and our simulations provide time-dependent values for temperature, velocity, and density at points throughout the wind. The information from each of these methods allows us to determine which parts of the wind are emitting X-rays, as well as the flux and velocity from each emitting zone. We then create theoretical line profiles by making histograms of the amount of flux emitted by material moving at each velocity within the range defined by the terminal velocity. We include not only the Doppler broadening of the lines from the velocity dispersion, but also the occultation by the star and attenuation of the emitted light by the equatorial cooling disk. The analytic line profiles are used to examine only the geometry of the wind, while the simulations are complete models of both

¹(http://cxc.harvard.edu/udocs/overview_cxo.html)

the geometry and kinematics of the wind. In addition to creating our simulations, we have observed θ^1 Orionis C using the *Chandra* satellite and have measured X-ray emission lines. Thus, we are able to compare our theoretical emission lines to the observed emission lines; through this comparison we examine the strengths and weaknesses of our model.

The next section will explain the reasons behind using the Doppler shifts, occultation, and absorption in creating our line profiles. Section 3 explains both the mathematics involved in accounting for these factors and the mechanics involved in rotating the observer’s frame with respect to a rotating star. The first part of Section 4 will explain our analytic models and the importance of absorption, Doppler shifts, and occultation. The second part of the section describes the post-processing of the MHD simulations. Throughout these sections we explain our motivations and any benchmarks we did in addition to the actual results. Section 5 describes the stellar parameters of θ^1 Orionis C, our observational data, and comparisons between our simulated line profiles and the observed X-ray emission lines. Finally, Section 6 includes our conclusions regarding both the comparison of the models to actual data and the general trends in the line profiles. It also discusses future work that needs to be done to better understand the role of magnetic fields in hot stellar winds.

2. Theory

The physical picture we model is that of a line driven wind that is confined by a dipole magnetic field. This is the case in both our analytic models and the profiles from post-processing output from hydrodynamic simulations. In many of these models, the field channels and confines the wind only out to the Alfvén radius, where the kinetic energy from the wind is greater than the energy of the magnetic field. At this point the magnetic field becomes open, with field lines flowing from the star. Figure 1 shows the original analytic MCWS model, and Figure 2 is an example of an MHD simulation of a dynamic MCWS model. This model forces the hot emitting wind to be in particular areas, namely near the equator, where the channeled wind collides. These shocks heat the wind to X-ray emitting temperatures. In addition to the radially flowing polar wind that is cool because it is never shocked, there is a cool equatorial disk of wind material that has been heated by the shock, and has cooled down by emitting X-rays. Once the material is cool, it is pushed into a thin disk by the new flow of material. Both of these cool areas of the wind can absorb X-rays that would otherwise reach the observer. However, by examining our MHD simulations we have found that the cool disk of material periodically empties as its material is pulled back to the surface of the star by gravity. Thus we believe that this cooling disk has little effect on the absorption of X-rays.

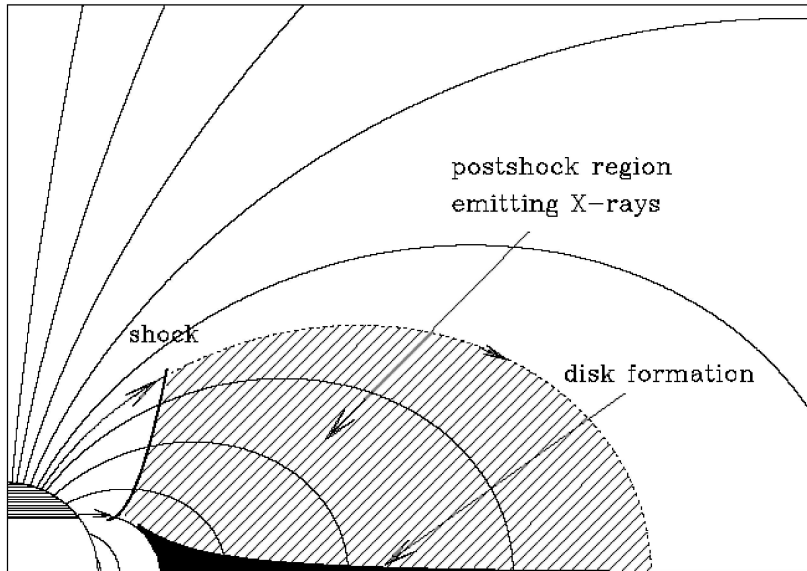


Fig. 7. Schematic view of the model proposed for the X-ray emission from IQ Aur (see text).

Fig. 1.— In this original MCWS model, described above by the original authors (Babel and Montmerle, 1997), the wind is forced to flow along the rigid magnetic field lines. The equatorial disk can be seen along the bottom and the shaded area is the hot emitting region.

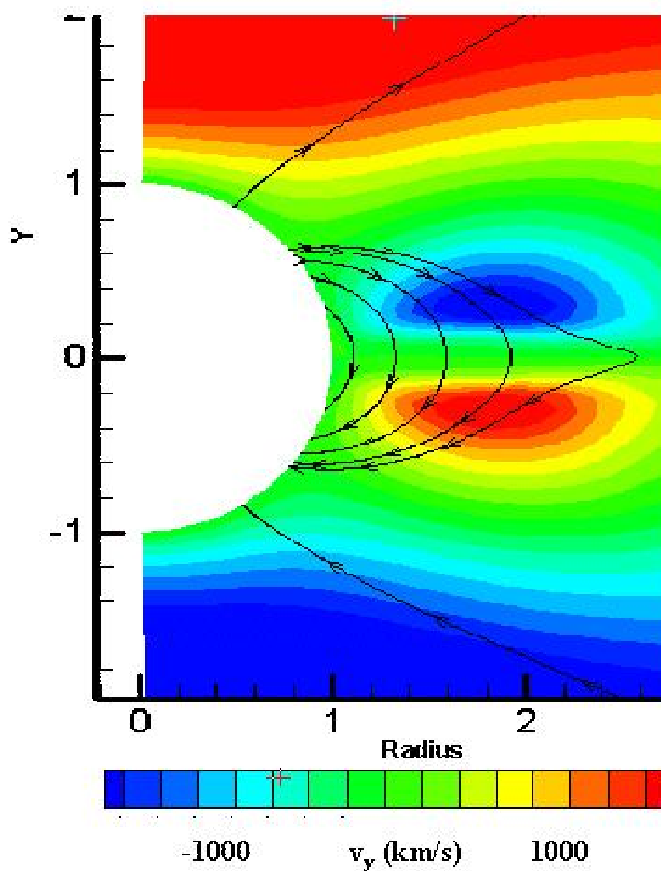


Fig. 2.— In this magnetohydrodynamic simulation, the field lines are stretched by the outflowing material. The color scheme describes the y -velocity of the outflow. The wind speeds up as it moves towards the equator where the opposing flows collide and heat the material.

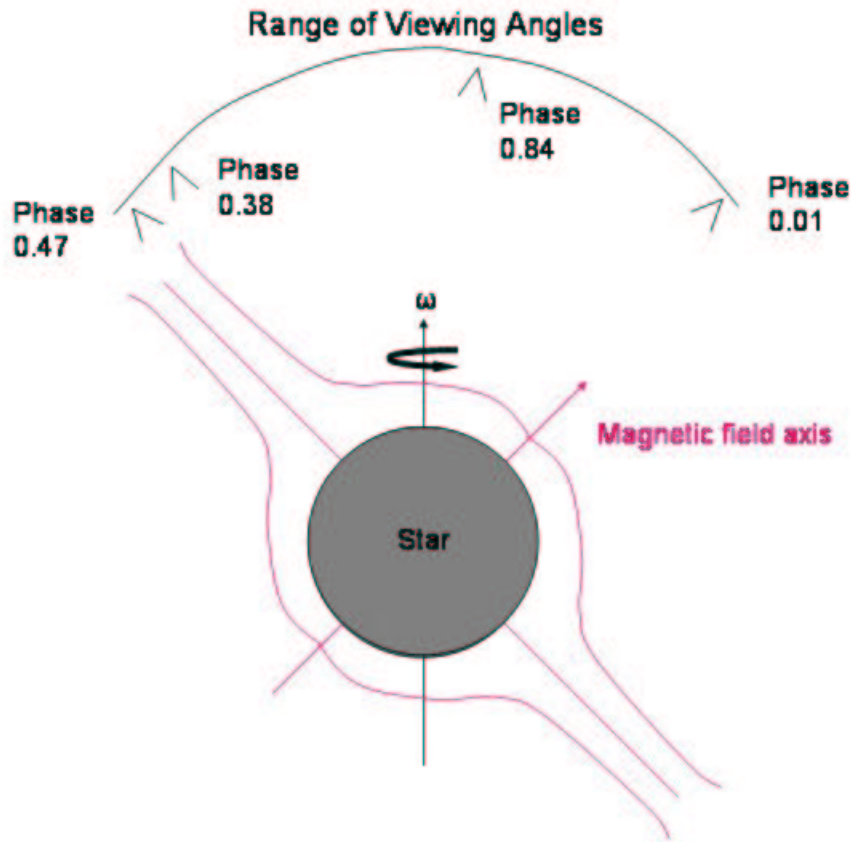


Fig. 3.— The misalignment of the rotational axis relative to the magnetic axis allows us to observe the star from all possible angles with respect to the magnetic axis. The angles from which we have data are labeled with the rotational phase. In ascending order corresponding to phase, the angles are, with respect to the magnetic field axis: 3.9, 79.6, 86.5, and 38.3 degrees.

An important assumption behind our work is that the shapes of the observed line profiles can be closely matched by our theoretical profiles by considering only kinematics and dynamics. This allows us to ignore any effects from the magnetic field other than containing and directing the wind flow, as well as specific atomic structure considerations. Wind absorption of X-rays, even for more dense winds, is much less than had been previously thought (Waldron & Cassinelli, 2001), so wind absorption will not be an important effect for θ^1 Orionis C. Although we do not yet consider specific ions yet in our emission lines, we do have some evaluation of temperature dependence in line profiles.

There are three effects that contribute to the analytically modeled line profiles. The first is the Doppler shift of the X-ray emitting wind; the second is continuum absorption and occultation; and the third is the observer’s viewing angle, which depends on rotation phase via the misalignment of the magnetic and rotational axes.

The Doppler shift of light is the perceived shortening or lengthening of its wavelength depending on whether the emitting object is moving towards or away from the observer. Because wind flows from the stars in all directions, an emission line that is centered at some rest wavelength becomes broadened in both the blue and red directions. The width is directly related to the velocity of the visible outflow.

$$\frac{\Delta\lambda}{\lambda} = \frac{v}{c} \quad (3)$$

However, some of the outflow may not be visible to an observer. The most obvious reason for this is that the star itself will block some of the wind. We assume that the wind it blocks is emitting the most redshifted light, so that should affect the symmetry of the line profile. Cool wind can also block or attenuate the light emitted by hotter wind. This is because the cool wind has atoms in a low energy state, and high energy light passing through the material may ionize the atoms rather than reaching the observer. As we mentioned previously, however, cool wind absorption has been found to be minimal in other stars with a higher mass-loss rate than θ^1 Orionis C (Waldron & Cassinelli, 2001).

The last important factor to take into account is the misalignment of the magnetic and rotational axes. This means that the observer is constantly viewing the magnetic field structure from a different angle, so different emitting plasma is being blocked by occultation and absorption at different times. In addition, this effect changes what material is emitting redshifted and blueshifted light. For example, in our analytic models, when the observer looks down along a magnetic pole, the cooling disk will attenuate much of the light from the lower hemisphere of the wind, and the polar wind will attenuate the emission from the upper equatorial shock. Occultation from the star may not have as much of an effect on the profile because hot wind is rare in the polar regions. However, when the observer is looking down

the magnetic equator, much of the hot, highly redshifted wind at the equator is occulted by the star, and the opacity of the cool equatorial disk and polar winds is unimportant, because little emission passes through that wind. Although it is the star that is rotating so that the orientation of the magnetic field is periodically changing with respect to the viewer, the effect is the same as if the eye of the observer were circling around the star. This can be seen in Figure 3. Although this effect is caused by the star’s rotation, so that the orientation of the magnetic field is continuously changing with respect to the observer, the same effect would result if the observer were circling around a stationary star.

3. Matching the Program to Theory

In this section we will discuss the steps involved in creating a stellar wind model from which we can calculate a line profile. This involves dividing a large spherical volume around our theoretical star into a grid. The density, velocity, and emissivity of the outflowing material are defined at the center point of each zone within the grid. In addition, we solve for a volume of each zone. The line profile is created by summing the total emission from each zone, which depends on the zone’s volume and density. We will also provide a description of the comparison of our model with a spherically symmetric analytic solution that will underline some important numerical effects. We will include one physical effect at a time as we build up and test our program.

Our program begins the gridding process by assigning evenly spaced r , θ , and ϕ gridpoints to a coordinate system aligned with the magnetic axis. This creates a three-dimensional grid on which all of our calculations are based. Every gridpoint has a corresponding radial velocity based on the β -velocity law, which is:

$$v(r) = v_{\infty} \left(1 - \frac{R_*}{r}\right)^{\beta} \quad (4)$$

This is an empirical law that has been found to match observations and is supported theoretically, with a β value of about one (Lamers & Cassinelli, 1999). Every point also has an assigned density that is proportional to $\frac{1}{vr^2}$; an emissivity that is proportional to the square of density, as $j = j_0 n^2$; and a surrounding volume element. By solving a general spherical polar volume integral, we find that each volume element size is:

$$vol_i = \frac{((r_{i-\frac{1}{2}} + rstep)^3 - (r_{i-\frac{1}{2}})^3)(\cos(\theta_{j-\frac{1}{2}}) - \cos(\theta_{j-\frac{1}{2}} + tstep))(\phi_{k-\frac{1}{2}} + pstep - \phi_{k-\frac{1}{2}})}{3} \quad (5)$$

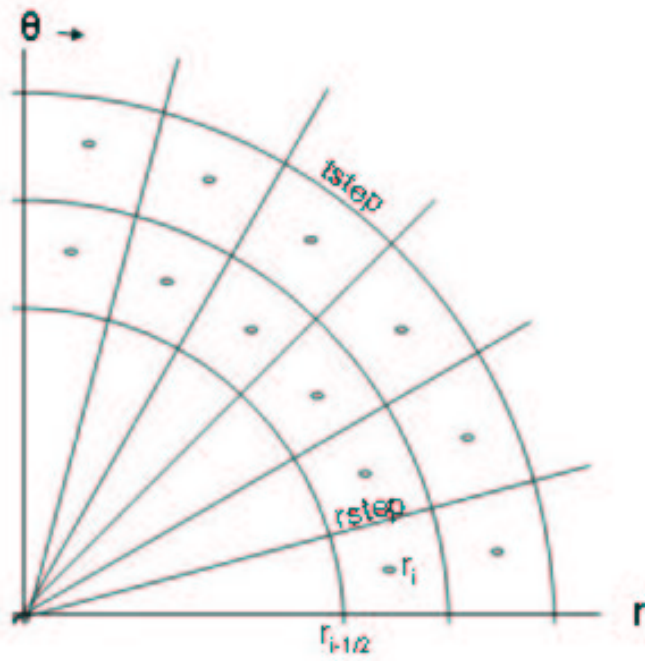


Fig. 4.— The lines in this grid mark the boundaries of the volume zones in the radial and θ directions. The center points are the points at which r , θ , and ϕ are defined. Volume elements in r and θ directions are bounded by the gridlines. Variation in the ϕ direction is perpendicular to the plane of the page, and is not shown in this diagram.

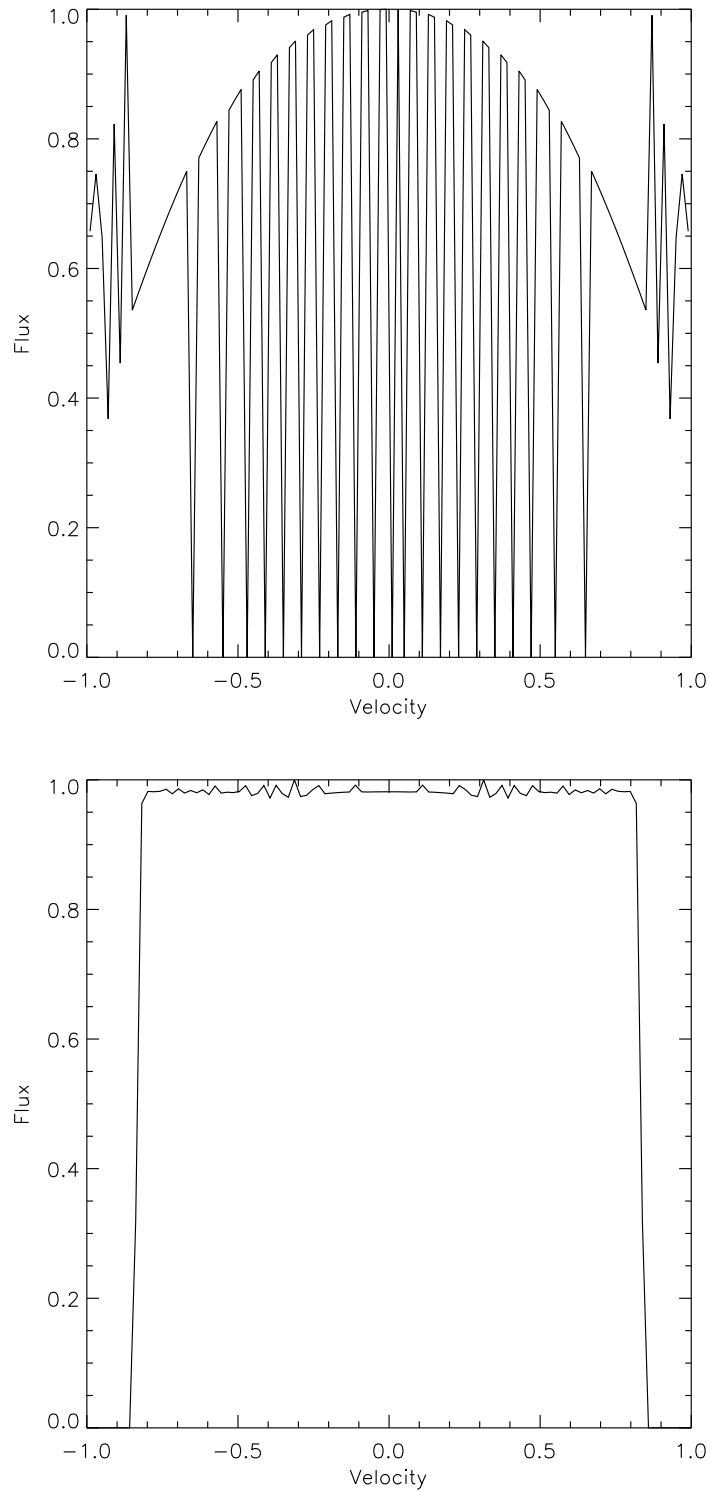


Fig. 5.— This figure displays the importance of using linear interpolation when binning. The second profile has a more realistically distributed velocity than the first because it uses interpolation. The x axis velocity is in terms of the fraction of the terminal velocity.

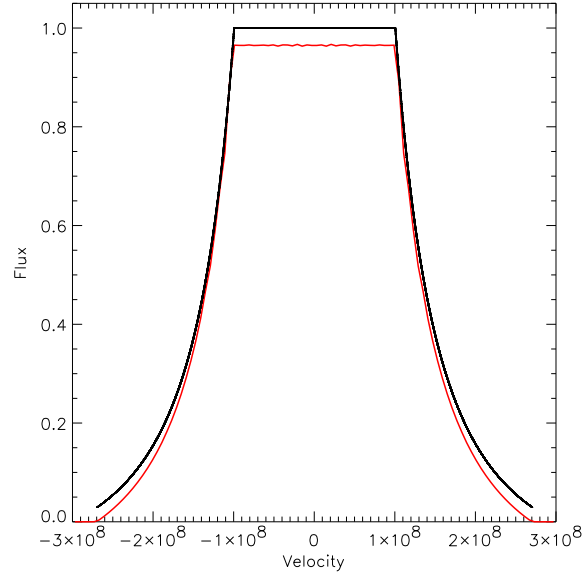


Fig. 6.— Comparison of our numerical solution (red) to the analytic solution (black). The program goes from 1.5 to 10 stellar radii in 90 steps.

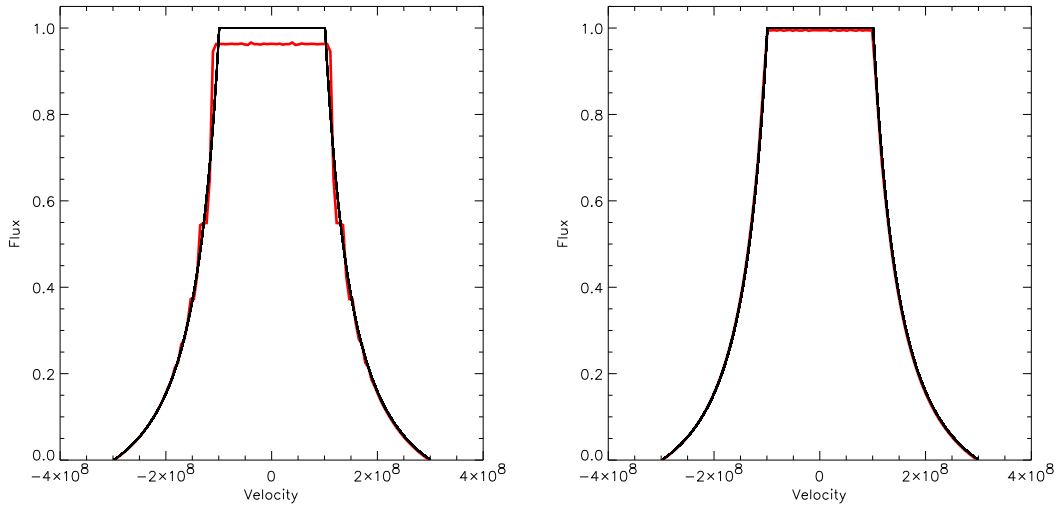


Fig. 7.— Line profiles comparing an analytic wind solution to our numerical model which integrates from 10 to 150 stellar radii, with 600 or 2000 shells. The profile with 2000 shells better matches the top of the analytic profile.

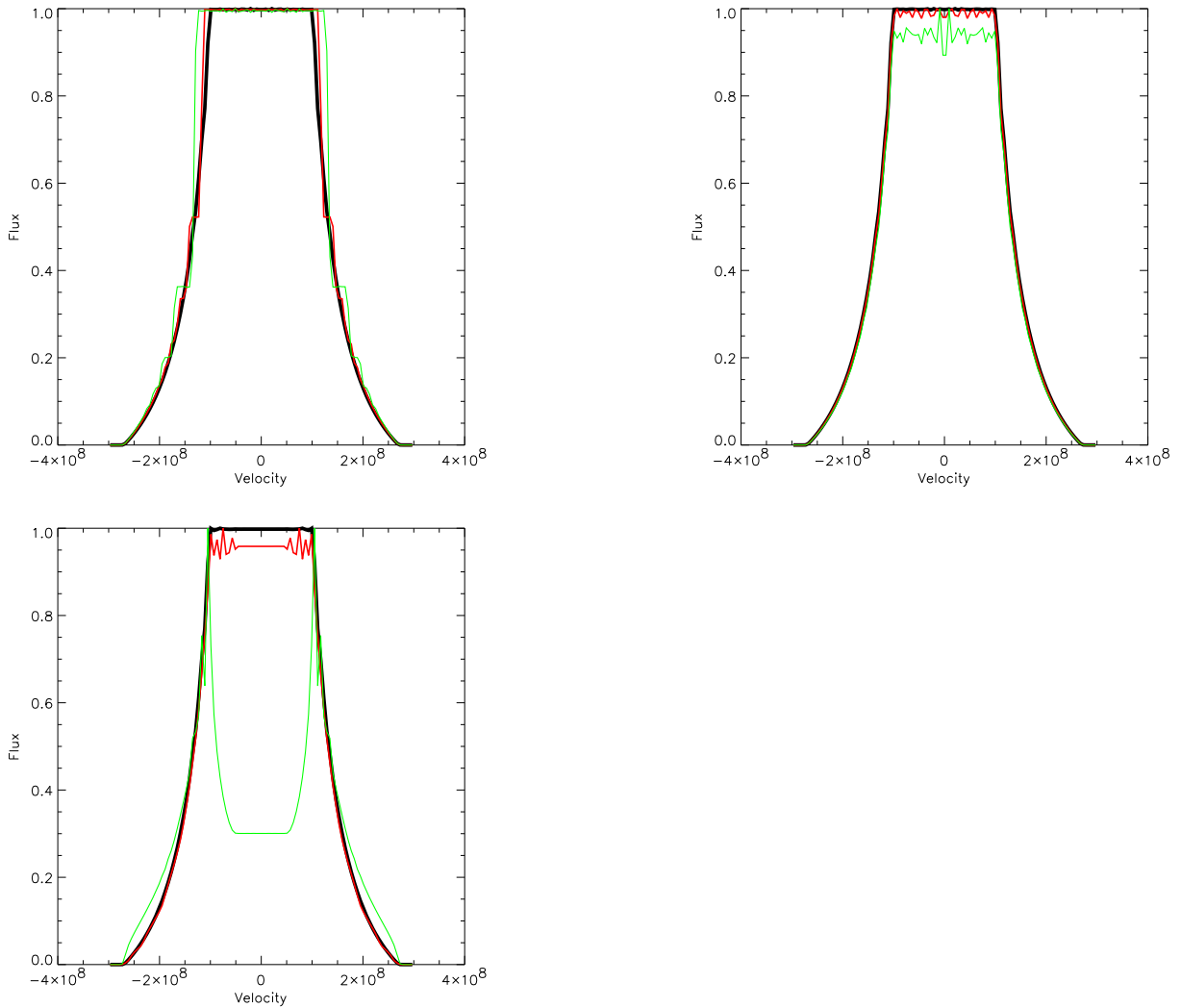


Fig. 8.— In clockwise order from the top left, the first plot shows 15, 30, and 90 shells. The second compares profiles with 60, 100, and 360 theta points, and the third graphs profiles using 2, 20, and 60 phi points at a viewing angle of 60 degrees. The green line always uses the fewest points and the black line uses the most.

where the values of the r , θ , and ϕ variables mark the sides of the volume elements. They are found by taking the midpoint between actual gridpoints in all three dimensions. The step variables ($rstep$, $tstep$, and $pstep$) are the size of the difference between consecutive edge variables, and are the same throughout the grid. This is illustrated in Figure 4. By multiplying the volume and emissivity from each grid point we are able to find the total emission from each volume element.

$$L = \int j d(vol) \tag{6}$$

In order to create a two dimensional line profile from this three dimensional set of data, the fluxes are organized according to line of sight velocity. Because the magnetic and rotational axes are not always aligned, the observer does not always view the system from the same angle. Thus we define a tilt angle, which is the distance in radians between the observer’s z-axis and the magnetic field’s z-axis. This is achieved by a rotation about the y-axis because the model is azimuthally symmetric. In order to find the line of sight velocities for any viewing angle, we perform the following coordinate transformation:

$$v_{los} = -(v_{x-mag})\sin(tilt) + (v_{z-mag})\cos(tilt) \tag{7}$$

where the velocities used in the calculation are the velocities in Cartesian coordinates in the magnetic field coordinate system. Finally, we sum the emission of all spatial zones corresponding to a given v_{los} value. This histogram of emission versus v_{los} is the line profile. Because we are unable to give every location in every volume element its own velocity, there can be noise in the profile from assigning the same velocity to an entire volume element. The finer our grid, the less noise is caused by this.

Our first benchmark of this program was to duplicate the known line profile of an outwardly accelerating spherically symmetric wind without occultation from the star. First we modeled a single spherical shell around a star. This should produce a rectangular line profile that is centered on the wavelength emitted by material moving at zero velocity with respect to the observer, with the edges at the observed wavelengths emitted by material moving at the speed of the shell directly towards and away from the observer. This widening of the profile is due to the first factor we take into account in our calculations, Doppler broadening. Because we assign our emission and velocity values to zones in a discrete grid, we cannot assume that there will be a continuous range of fluxes. Thus integrating the emission over the velocities would result in a very jagged profile that would have many velocities with no flux. Our solution is to choose a number of velocity bins in which to sum the line of sight velocities. Our first attempt summed all the emission from a spatial zone into the bin that contained the velocity of the grid point. This did not take into account the

possibility of a velocity being close to the boundary of a bin, and resulted in a jagged profile that was not rectangular (Fig 5). We use a linear interpolation in which the emission is split according to the center gridpoint velocity’s proximity to the two nearest bin centers. The amount of emission put into each bin is proportional to the difference between the velocity of the grid point and the velocity of the bin center. Figure 5 shows two line profiles that display the smoothing from this interpolation scheme. Using the interpolation, the program produced the expected box shape.

The next analytic test is that of a complete wind with concentric layers of accelerating shells. Since each single shell produces a rectangular line profile, the profile created from a number of shells can be represented by a number of rectangles of varying widths. The maximum width is from the outermost layer where the wind has reached its terminal velocity, and the minimum width is that of the flat top, whose limits are defined by the velocity of the innermost emitting wind. The analytic line profile contains an infinite number of thin shells whose emission results in thin rectangular profiles. This creates a smooth curve from rectangle corner to corner connecting the innermost top edge to the outer bottom edge. In order for our model to match the solution, we need many closely spaced shells. In Figure 6 the wings of our numerical model do not match the analytic solution because the numerical model sums emission to only ten stellar radii. One hundred fifty stellar radii are necessary for a complete match. In order for the top of the line profiles to match there needs to be a large number of shells. This is because of the way our program calculates the velocity of a shell. Even if the innermost shell begins at the same radius as the analytic model, the velocity is not calculated until the center point of the shell is reached. If there are few shells of large radial width, this velocity can be at a very different radius than the beginning emitting radius. Increasing the number of shells in a radial range decreases the shell width, so the velocity is calculated at a radius closer to the inner radius. When we use 2000 shells spanning 1.5 to 150 stellar radii, our profile is a close match to the analytic profile (see Figure 7).

Finding the best fit to the analytic profile included finding the number of grid points that are necessary in the three coordinates, r , θ and ϕ , to cause a smooth profile. The number of shells, or r grid points, is important to the height and to the appearance of the sides of the profile. With increasing numbers of shells, the sides of the profile become smoother until the curve looks more like an integration over the wind than a sum over discrete shells. This integrated appearance occurs when about ninety gridpoints are used in a wind to 10 stellar radii (Figure 8). In a system viewed along the pole, the number of theta gridpoints dictates the noise in the horizontal top of the profile. About 700 θ grid points are necessary for a smooth profile. Once the viewing angle has moved from the magnetic pole, and thus the tilt value is greater than zero, the number of ϕ points becomes more important, and about 60 ϕ

points are necessary for a smooth top (Figure 8).

The next effect we account for in our model is occultation by the star. In an otherwise spherically symmetric emitting wind, this would block only the most redshifted emission, causing an asymmetric profile. In our program, a zone is occulted if its center gridpoint has both a negative z component and $(x^2 + y^2) \leq 1$ in the observer’s coordinate system, where the variable values are in terms of R_* . As expected, Figure 9 shows attenuation only on the red side of the profile. In all of the models we will describe, occultation by the star affects the line profile.

Our program often switches between Cartesian and polar coordinates in order to facilitate the consideration of different viewing angles. This is because we consider a spherically symmetric wind with a radial outflow, but calculate the line profile based on the velocity in the z -direction of the observer oriented axis. Note from equation 7 that the line of sight velocity is calculated using the Cartesian velocities from the magnetic axis. However, our β -law velocity equation (equation 4) calculates a radial velocity, and eventually we will take a θ and ϕ velocity into account. There are three steps to changing a vector in polar coordinates into a vector in Cartesian coordinates. First, we consider a vector in spherical polar coordinates. We then find the Cartesian component of each of the polar coordinates and sum them to find the Cartesian vectors.

$$v_{polar} = v_r \cdot \hat{r} + v_\theta \cdot \hat{\theta} + v_\phi \cdot \hat{\phi} \quad (8)$$

$$\begin{aligned} \hat{r} &= \hat{x}\cos\phi\sin\theta + \hat{y}\sin\phi\sin\theta + \hat{z}\cos\theta \\ \hat{\theta} &= \hat{x}\cos\theta\cos\phi + \hat{y}\cos\theta\sin\phi - \hat{z}\sin\theta \\ \hat{\phi} &= -\hat{x}\sin\phi + \hat{y}\cos\phi \end{aligned} \quad (9)$$

$$\begin{aligned} v_x &= v_r\cos\phi\sin\theta + v_\theta\cos\theta\cos\phi - v_\phi\sin\phi \\ v_y &= v_r\sin\phi\sin\theta + v_\theta\cos\theta\sin\phi + v_\phi\cos\phi \\ v_z &= v_r\cos\theta - v_\theta\sin\theta \end{aligned} \quad (10)$$

We can then calculate the line of sight velocity using the previous equation. We verified that in a spherically symmetric wind, the line profiles from every angle are exactly the same.

By comparing our output to known analytic equations we were able to verify that our program correctly manipulates Doppler shift, occultation and viewing angle. In order to produce emission lines with an integrated shape rather than a sum of discrete shells it is necessary to include 90 r zones, 600 θ zones, and 60 ϕ zones. We use grids of roughly these dimensions for all of our models, as described below.

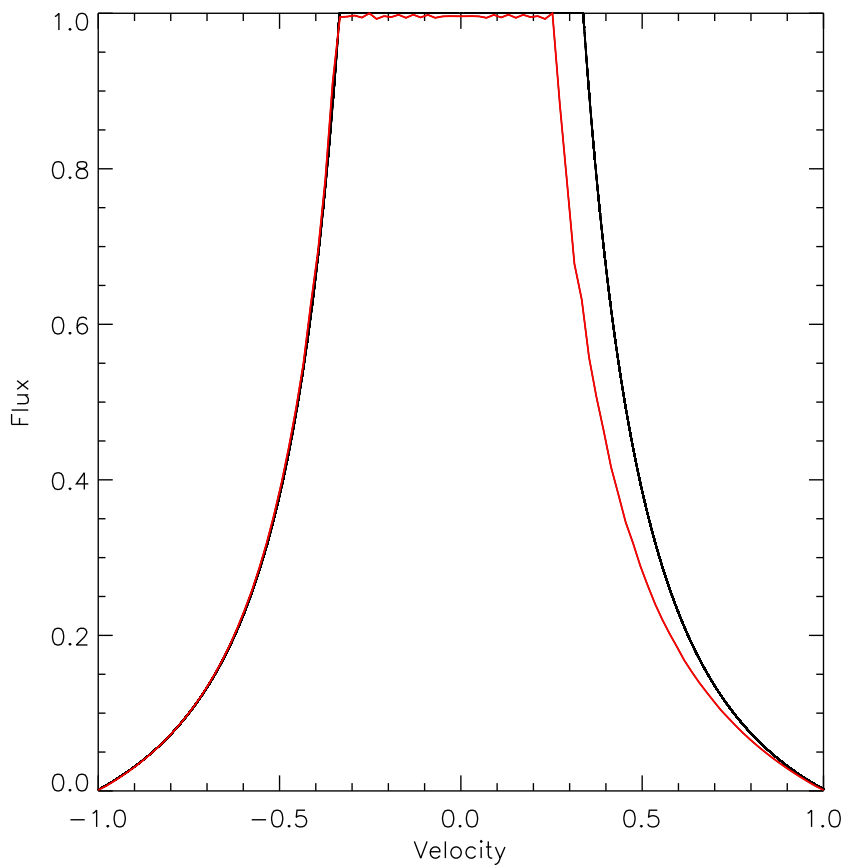


Fig. 9.— The occulted line profile (red) in comparison with the analytic profile (black). The redshifted emission is occulted.

4. Models

4.1. Analytic Models

4.1.1. Equatorial Radial Outflow

Our first model is a straightforward radial outflow as described by equation 4. This model is a variation on the completely spherical emitting wind. It is also the most simple portrayal of an emitting equatorial wind. We set the emissivity to zero for all but the volume between the θ values of 70 to 110 degrees. Because the emitting volume is dependent only on the value of theta, this model looks like a flared disk (Figure 10). In addition, because the emissivity of a zone is proportional to the density squared, we let only the zones outside of $r = 1.5R_*$ emit. This stops the emission from that small inner volume from dominating the entire profile due to the high density near the star. Strong shocks very close to the star are not likely because the material moving along the magnetic field lines would not have time to accelerate to high velocities before being shocked at the equator.

This model is an estimate of the geometrical emitting zone in the MCWS model rather than an attempt to describe the velocity profile of a magnetically confined wind. The emitting area begins to widen as it gets further from the star, which roughly corresponds to the shocked material in Figure 1. However, in this analytic model the emitting wind continues to widen out to the edge of the wind, which does not match the expected structure of the MCWS shock zone, because the shocked emitting wind must be inside the Alfvén radius. Wind far from both the star and the equator is unlikely to be a strong emitter in the actual MCWS model, but can emit in this analytic disk model. We also have a density that is dependent solely on radius, and so wind that is linearly far from the equator but the same radial distance from the star will emit as much as wind that is close to the equator. The most important distinction between this flared disk model and the MCWS model in terms of the line profiles is that between the velocity profiles. The analytic disk model has a completely radial velocity, while the MCWS model channels the wind along the field lines of the dipole magnetic field, resulting in a velocity with both radial and altitudinal components.

This model originally had no occultation or absorption, and the results were as expected for a wind with such a structure. The line profile as viewed from the magnetic pole is narrow because all of the wind is traveling at a large angle from the line of sight (see equation 7) so even wind with a fast speed has a small line of sight velocity. As the viewing angle increases towards a view parallel to the magnetic equator the line profiles become more broad and begin to have a dip in the flux at the zero line of sight velocity. The breadth of the line results from emitting wind traveling directly towards or away from the viewer and the line

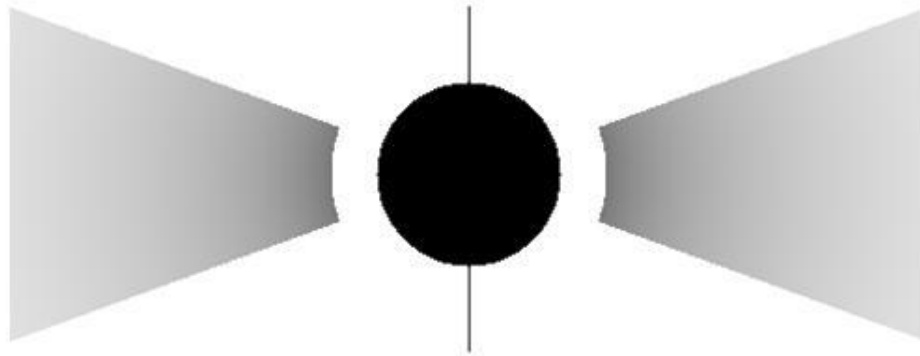


Fig. 10.— This is a two dimensional cross-section of the flared disk model. Density decreases with distance from the star, and therefore emissivity does as well.

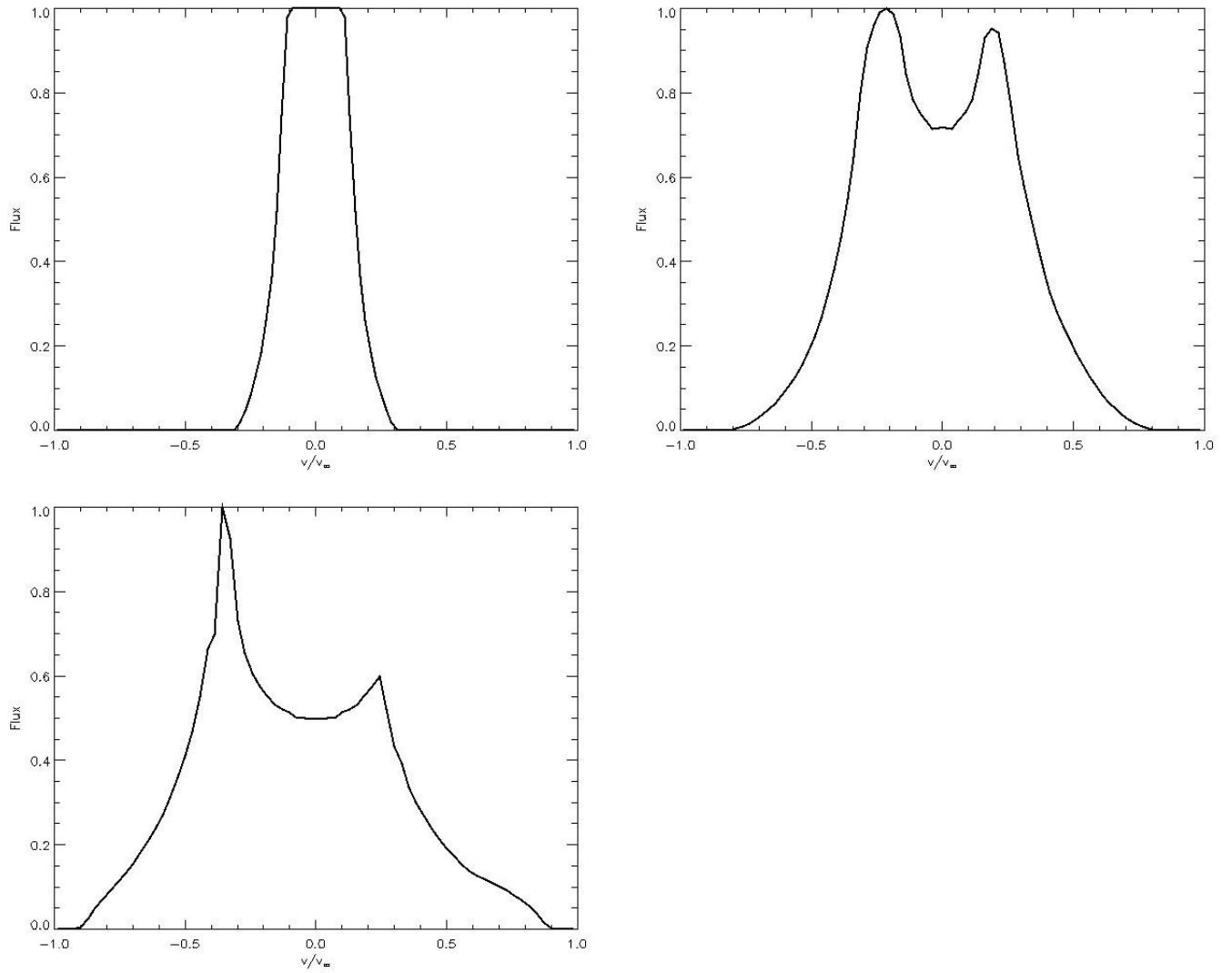


Fig. 11.— These are the equatorial outflow models with occultation. The viewing angles are at the pole (upper left), 45 degrees from the pole (upper right), and the equator (lower left).

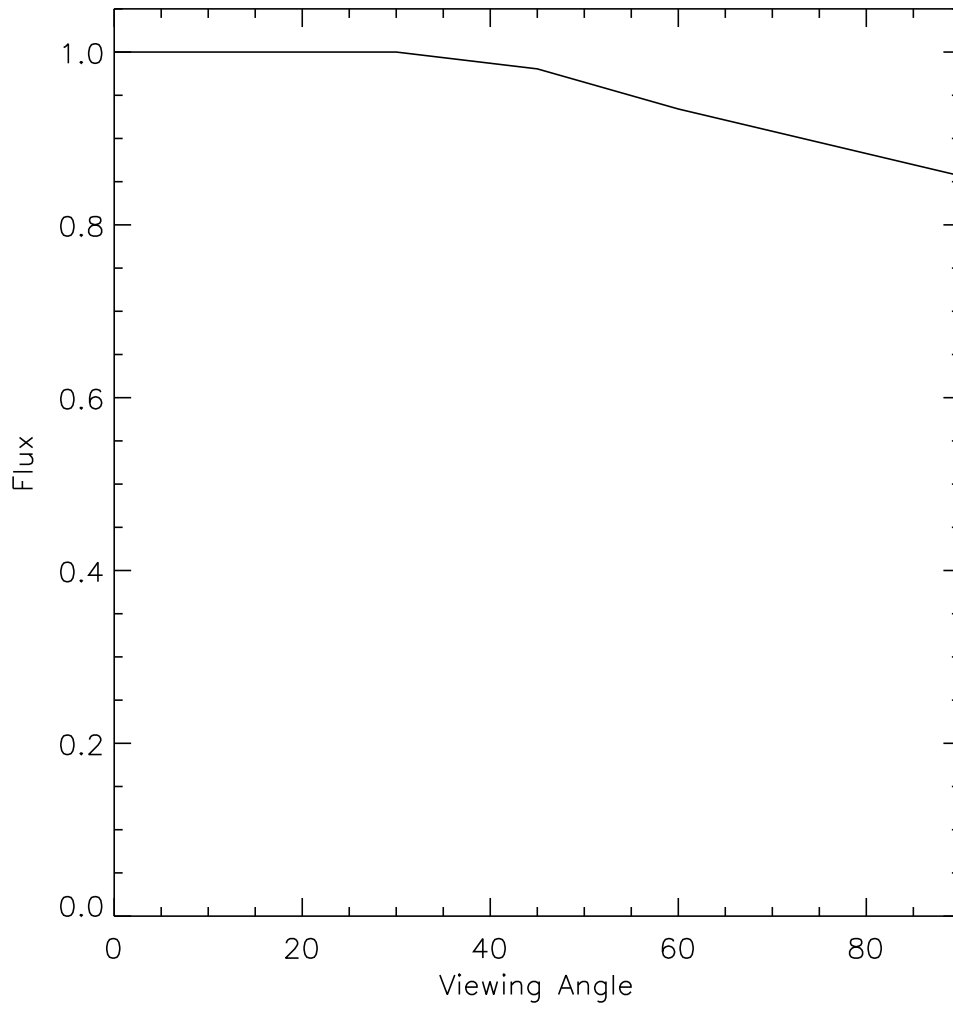


Fig. 12.— The lightcurve of the flared equatorial disk model. The flux is normalized to the maximum total emission. Note that flux decreases with increasing viewing angle.

of sight rotates towards the equator, and the dip comes from the fact that as viewing angle increases less emitting material is flowing perpendicularly to the line of sight because the polar outflow is too cool to emit X-rays. At the equatorial viewing angle the flux at zero velocity is emitted from wind that is in the equatorial plane but still perpendicular to the line of sight.

The addition of occultation to this model blocks an increasing amount of emission with increasing viewing angle. From three originally symmetric lines, Figure 11 shows the increasing effect on the profiles by occultation with increasing viewing angle. The figures show that there is no change to the pole-on view, while there is significant attenuation at the redshifted side of the line profile in the equatorial view. This can also be seen by examining Figure 12, which plots the flux at difference viewing angles in a lightcurve of the model.

4.1.2. Flared Models with an Azimuthal Velocity Component

The next addition we made to our analytic model was to consider an azimuthal velocity. We retained the radial velocity that existed in the original model, and simply added an azimuthal component. First we considered the types of rotational velocity that might be occurring in a wind. We examined three types of rotation: Keplerian rotation, solid body rotation, and an angular momentum conserving rotation. This gave us three equations. The Keplerian velocity is used to describe objects orbiting a larger mass:

$$v_{\phi} = \sqrt{\frac{GM}{r}} \quad (11)$$

The solid body velocity assumes that the entire wind moves with the star as a rigid mass:

$$v_{\phi} = \omega r \quad (12)$$

The conservation of angular momentum assumes that any piece of material leaving the star must always have the same momentum, no matter how far it gets from the star:

$$v_{\phi} = \frac{\text{constant}}{mr} \quad (13)$$

or mass may be expressed in terms of density:

$$m = \rho(\text{vol}) \quad (14)$$

$$v_{\phi} = \frac{\text{constant}}{\rho r(\text{vol})}$$

The line profiles for the models with an azimuthal velocity are shown below. When seen from a polar line of sight, the azimuthal disk model has the same line profile as the

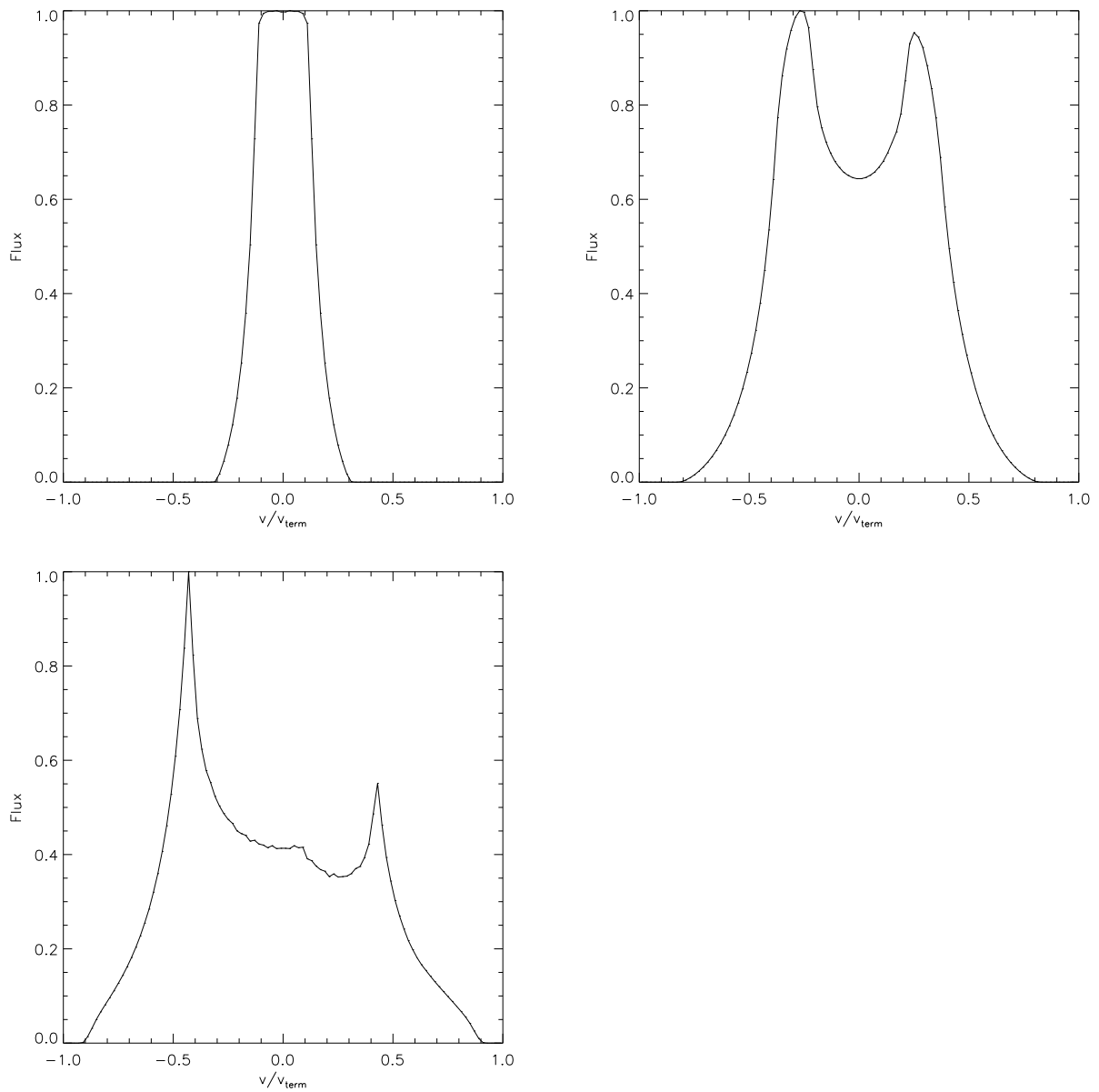


Fig. 13.— These are occulted views of a model with a Keplerian azimuthal velocity. The viewing angles are: polar (upper left), 45 degrees (upper right), and 90 degrees (lower left).

purely radial outflow. This is because the azimuthal component is perpendicular to the line of sight. The largest differences between the line profiles from the completely radial outflow as shown in Figure 11 and from the azimuthal model in Figure 13 are seen at an equatorial view.

Considering the differences between a purely radial outflow and material with both radial and azimuthal velocities is important for a general picture of the effects on line profiles of the addition of different velocity directions. Like the radial outflow model, the wind velocity structure does not mimic that of the MCWS model. Also, since we are currently using all of our models for comparison with data from θ^1 Orionis C, which has a long rotational period of 15.4 d (Donati et al, 2002), further study of the differences between rotational models was left for future work. This long period means that the material flowing from the star would not have a large azimuthal velocity. The fastest azimuthal velocity would be obtained from wind that was corotating with the star, if, for example, the magnetically confined wind were turning with rigid field lines attached to the stellar surface. However, because the period is so long, the velocity of the outflow would not be drastically affected even by the rigid rotator model. We also find that the general shapes of the line profiles from the model including azimuthal velocity do not differ drastically from those created by the equatorial model with a purely radial flow.

4.1.3. Dipole Model

Our final analytic model is the only analytic model that is comparable to the MCWS model in its kinematics. In this model only the material within a dipole region emits X-ray photons. This model is similar to the Babel and Montmerle (1997) model in that the dipole field lines never change in reaction to the force from outflowing material (Figure 1). We calculate the speed of the material based on the radial distance from the star using the β -velocity law, as in our other analytic models. We then add channeling from the magnetic field lines by splitting the total speed into a radial and θ component based on the ratio of the magnitudes of the magnetic field in the radial and θ directions. The equation for the magnetic field of a dipole is:

$$B(r) = \frac{\mu m}{4\pi r^3} (2\cos\theta\hat{r} + \sin\theta\hat{\theta}) \quad (15)$$

We choose the emitting wind to be within the field line that reaches $3 R_*$ at a θ angle of 90 degrees, the magnetic equator. We choose this value because $3 R_*$ is roughly the Alfvén radius. This model includes not only r and θ directions in the wind, but also a cool equatorial disk. Emitted light can be blocked both by occultation, and by our assumed "cooling disk,"

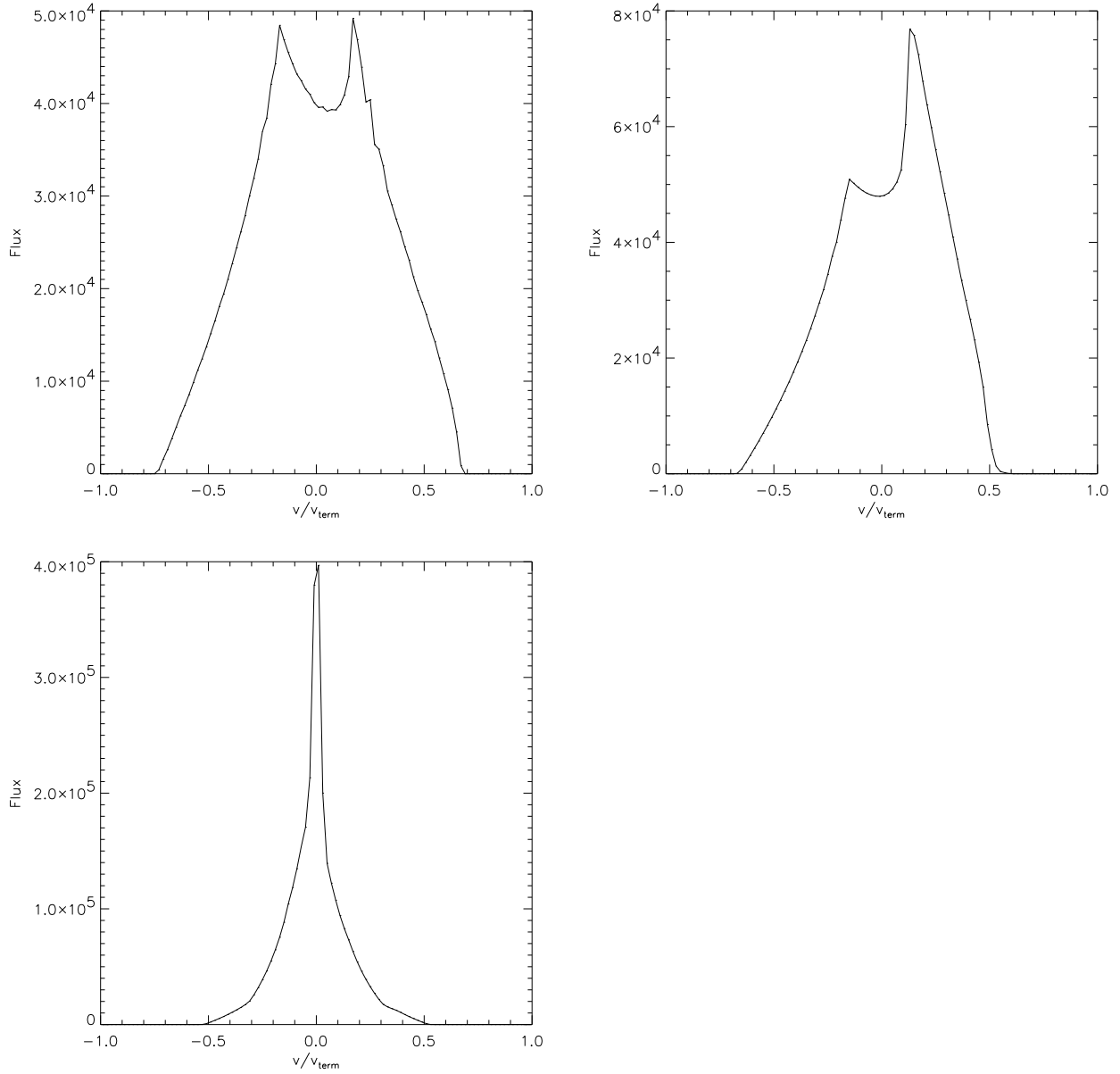


Fig. 14.— The line profiles above are from a dipole model whose field goes from $1.2 R_*$ to $3 R_*$. The viewing angles are polar (upper left), 45 degrees (upper right), and equatorial (lower left). Notice that the y axes have different ranges such that the equatorial profile has the most flux at its peak.

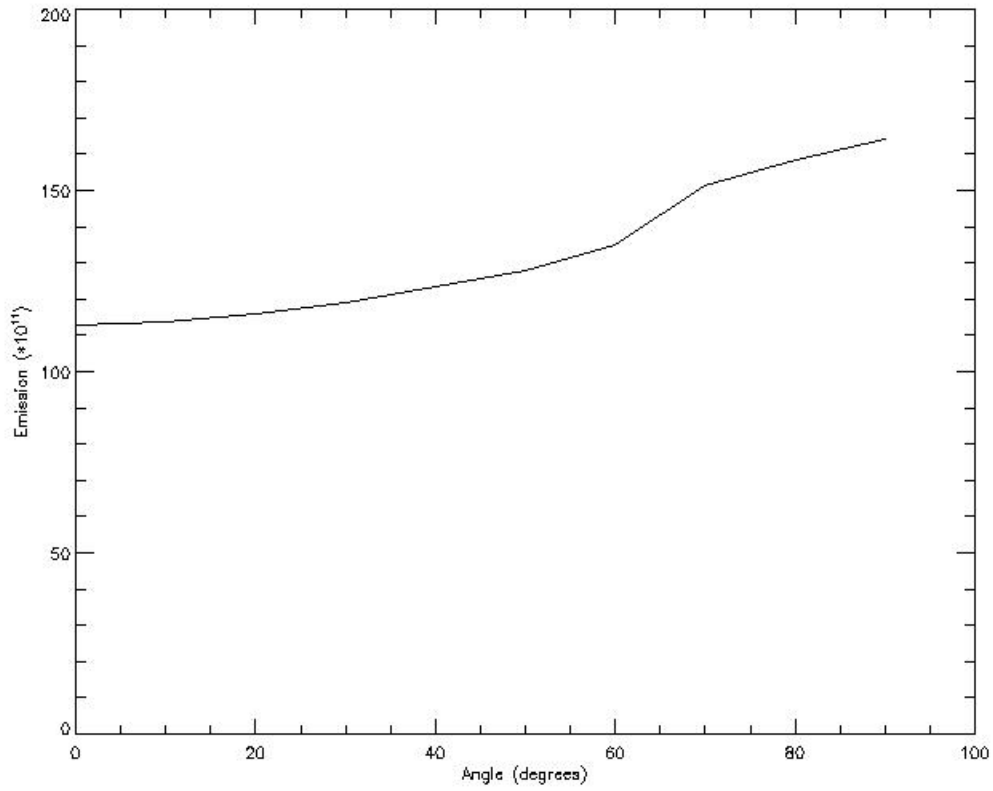


Fig. 15.— This is the lightcurve from the dipole model with disk absorption. Notice that the light reaching the observer increases with the viewing angle.

which is completely optically thick out to $3 R_*$, and completely optically thin beyond that. We program this by finding all the grid points whose emission must cross the equatorial plane to reach the observer. By setting the emissivity of all these points to zero, we bypass calculating the physical process of absorption:

$$\begin{aligned} I_{abs} &= I_o e^{-\tau} \\ \tau &= \int \rho \kappa ds \end{aligned} \tag{16}$$

Programming this exact physical process is difficult because it involves interpolating the spherical grid around the magnetic axis into a cylindrical grid around the observer’s axis, as will be explained in Section 6.

Combining these two additions to our analytic model, we find large differences in both our line profiles and our light curve. In the dipole model’s line profiles, the lines become narrower with increasing viewing angle (Figure 14), whereas in our radial outflow models the lines broaden with increasing viewing angle (Figure 11). This results from the two-dimensional directionality of the dipole channeled outflow. The asymmetry in the profiles results from the cooling disk. The line profile as viewed from the equatorial axis is symmetric because the cooling disk does not block any emission.

Comparing the light curves in Figures 12 and 15, we find a trend in the opposite direction: in the dipole model the equatorial disk dominates occultation by the star, whereas in the radial outflow model only occultation blocks emission. The dipole model’s cooling disk blocks the most light when the viewer is looking along the pole, and the radial outflow model occults the most emission when the viewer looks along the magnetic equator.

4.2. Post-Processing Magnetohydrodynamic Simulations

4.2.1. Magnetohydrodynamic Simulations

Magnetohydrodynamic (MHD) simulations are useful because by setting starting conditions such as the radiation force and the surface temperature of a star, one can observe the system changing with time. Using the MHD simulations calculated by ud-Doula and Owocki (2002) and some custom-calculated for this project, we were able to create more realistic models of line profiles. An important parameter in this model is η , which is the ratio of the kinetic energy from the wind to the energy in the dipole magnetic field. This parameter is used to calculate where the magnetic field is closed, and thus where the shock zones are. η is calculated using a simple equation, taking the ratio of the kinetic energy of

the wind at some point in the wind, as calculated using the β -velocity law, and the dipole field strength, which is inversely proportional to r^3 . When this ratio is equal to one, the wind energy has overpowered the dipole field strength and the field lines will be open. This program outputs data on a fine two-dimensional mesh. At each point there are calculated values for density, temperature, and x and y velocities. By modifying our program from one that created analytic models into one that inputs data from the MHD simulations, we were able to create line profiles.

The MHD simulations are two dimensional with an assumed azimuthal symmetry. In order to produce a smooth line profile, we rotate this two dimensional grid in the phi direction with sixty ϕ zones, the number of ϕ zones necessary for a smooth profile at any viewing angle. Because there is no steady state result of the MHD simulation, our assumption that the model is the same in every azimuthal direction is a simplification that may not reflect reality. In the future we will use a method similar to the "soccer-ball" method of Dessart and Owocki (2002). Rather than using the same moment of the two dimensional model in all of our ϕ slices we would use different times at different slices, effectively creating a three dimensional simulation out of this two dimensional simulation.

4.2.2. Isothermal Models

The first MHD simulations that we used included only mass and momentum conservation equations. The hot gas has no equation of state to force hotter gas to have a high pressure and expand. This means that the hot gas is able to stay in a very thin region right at the equatorial plane, as in ud-Doula and Owocki (2002).

Emission from an Equatorial Region

Because isothermal models do not explicitly calculate temperature, we can only use crude methods to determine which zones emit X-ray photons. Our first method used a completely spatial criterion based on our assumption that only wind in the equatorial region will be hot enough to emit X-rays. This model is similar to our analytic equatorial outflow model because we assume that all the material within a certain θ range around the magnetic equator is emitting X-rays. In this model we assume that all material within 10 degrees from the equator emits X-rays.

The model we use to create these line profiles has only 10 ϕ angles. We did this in order to decrease the program's running time. However, examining the line profiles produced by the method in Figure 16, one can see that the resolution has created a spiky appearance

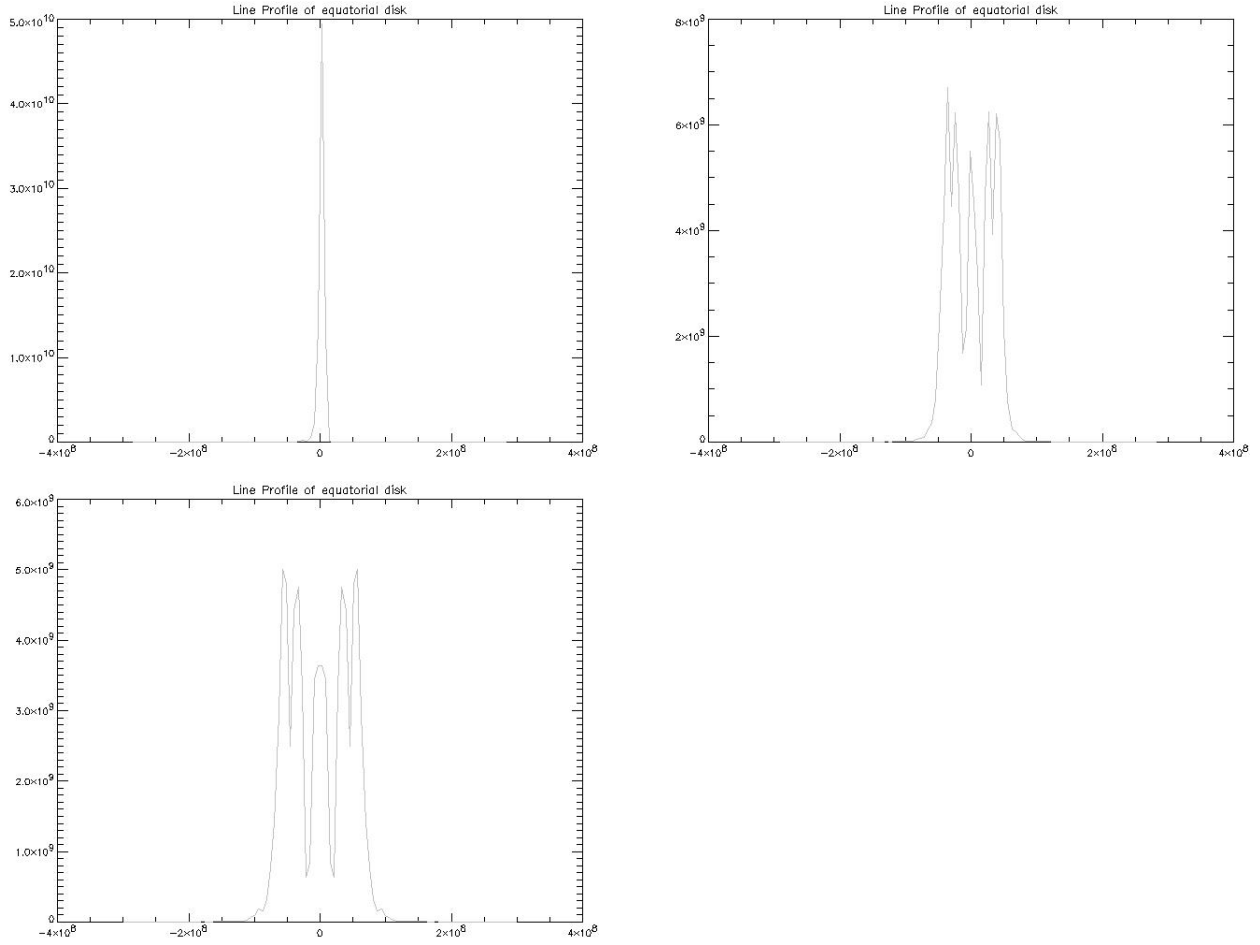


Fig. 16.— This model has emission from the wind everywhere within 10 degrees from the equator. Note the similarity of the general shape to the general shape of the equatorial outflow. Polar view (upper left), 45 degree (upper right), and an equatorial view (lower left). There is no occultation from the star.

that is not seen in any of the analytic models. The analytic models ran with at least 60 ϕ zones, the minimum number of ϕ zones we found necessary to create a smooth profile at any viewing angle. In addition, some of the spiky appearance may be due to the numerical nature of the MHD simulations. As seen by comparing Figure 11 to Figure 16, despite the lack of resolution, the general shape of the profiles mimics that of the equatorial outflow line profiles. The width increases with viewing angle, and there is a dip at zero line of sight velocity at the higher viewing angle.

4.2.3. *Non-isothermal Model*

The more realistic MHD simulations that we used, which were calculated for this project for the first time, included an energy conservation equation in addition to the mass and momentum conservation equations. This means that temperature was explicitly calculated rather than determined from a steep velocity gradient. Because temperature is proportional to pressure as described by the ideal gas law, the increased temperature of shocked gas can cause it to expand and emit X-rays in a thick region around the magnetic equatorial plane. This also means that as the collisionally heated gas radiatively cools it condenses into a dense cooling disk. However, we found that this cooling disk is not as stable as we expected; at some point, enough cool gas collects on top of a magnetic field line that the material is dragged back onto the star by gravity. It does not break the field line, however, and so "snakes" back to the stellar surface. This process can be seen in greater detail in movies that have been made by ud-Doula and can be found on the web ².

Emission from Hot Zones

This model has no absorption from the wind, and all wind at or above 10^6 K emits X-ray photons (later we explore the effects of changing this temperature criterion). We use the equation of state in this model that explicitly calculates the temperatures for each zone, rather than estimating the temperature from velocity gradients as we would need to do in the isothermal models. The use of our binning technique smears the line profile and makes some of the details more difficult to see, making our modeled line profiles more comparable to *Chandra* observational data, which have limited spectral resolution. However, the smoothing in our simulated line profiles is not as dramatic as the smoothing in the *Chandra* data; our bin size is about 75 km s^{-1} , while *Chandra* has a resolution of about 300 km s^{-1} .

²at <http://astro.swarthmore.edu/~cohen/stephanie/mov.html>

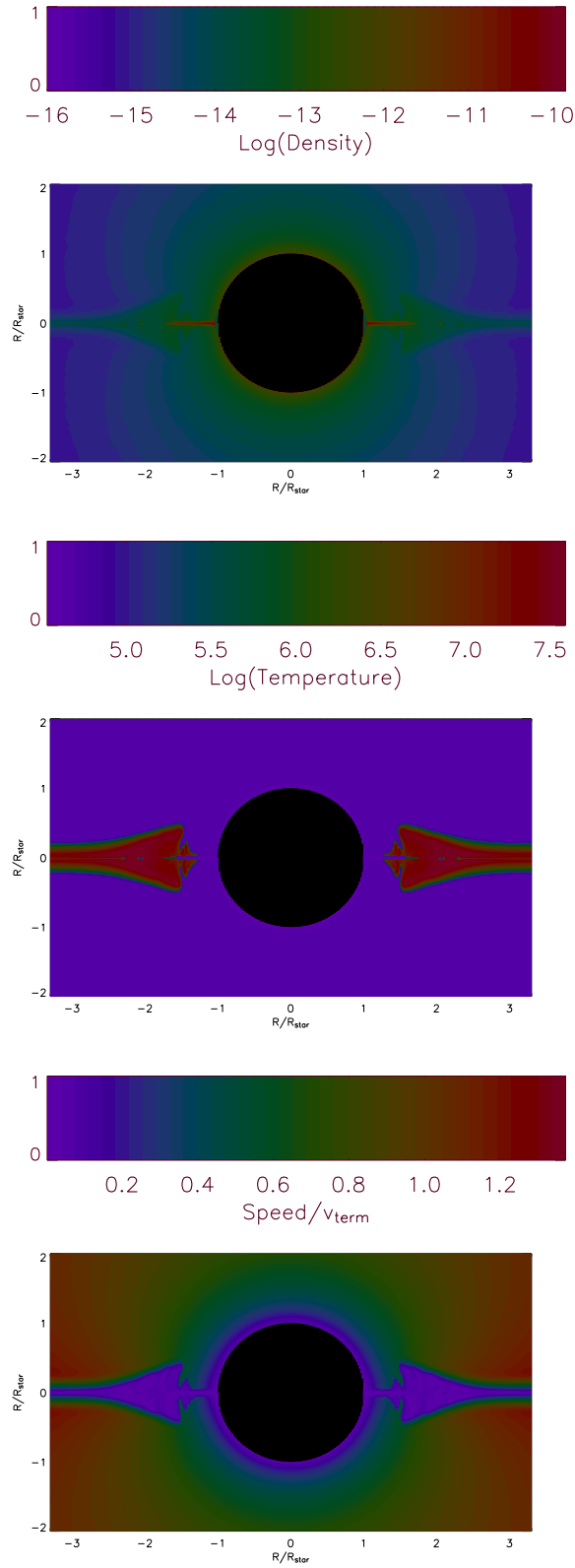


Fig. 17.— Above are three contour plots for a polar symmetric time in the MHD simulation. (top) is the density contour plot, (middle) is the temperature contour, and (bottom) is the contour of speed. Note the the speed contour does not take directionality into account

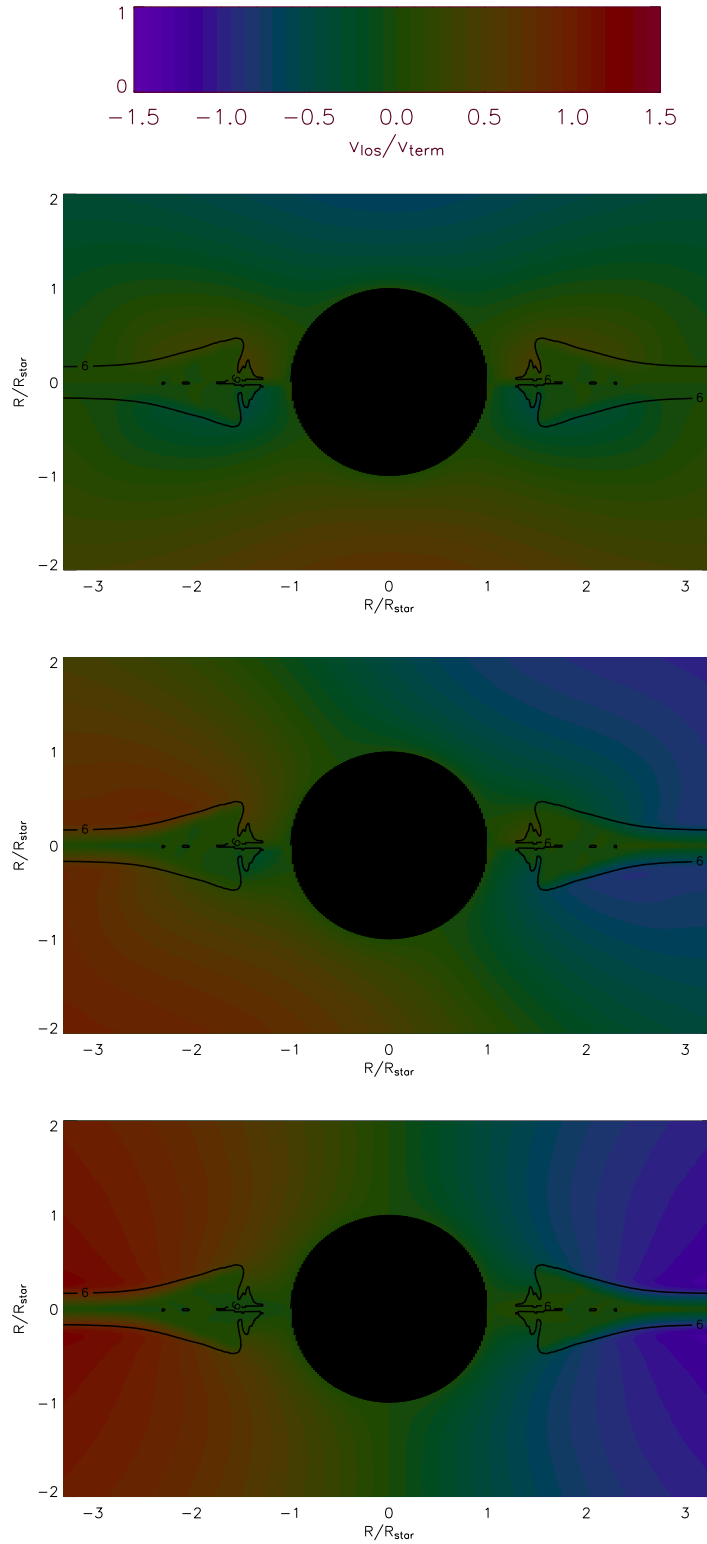


Fig. 18.— Above are the three contour plots from the line of sight velocity. The terminal velocity has been chosen to match the velocity stated in Donati et al (2002) of 2500 km/s. (top) Is the polar view, (middle) the mid-view, and (bottom) the equatorial view.

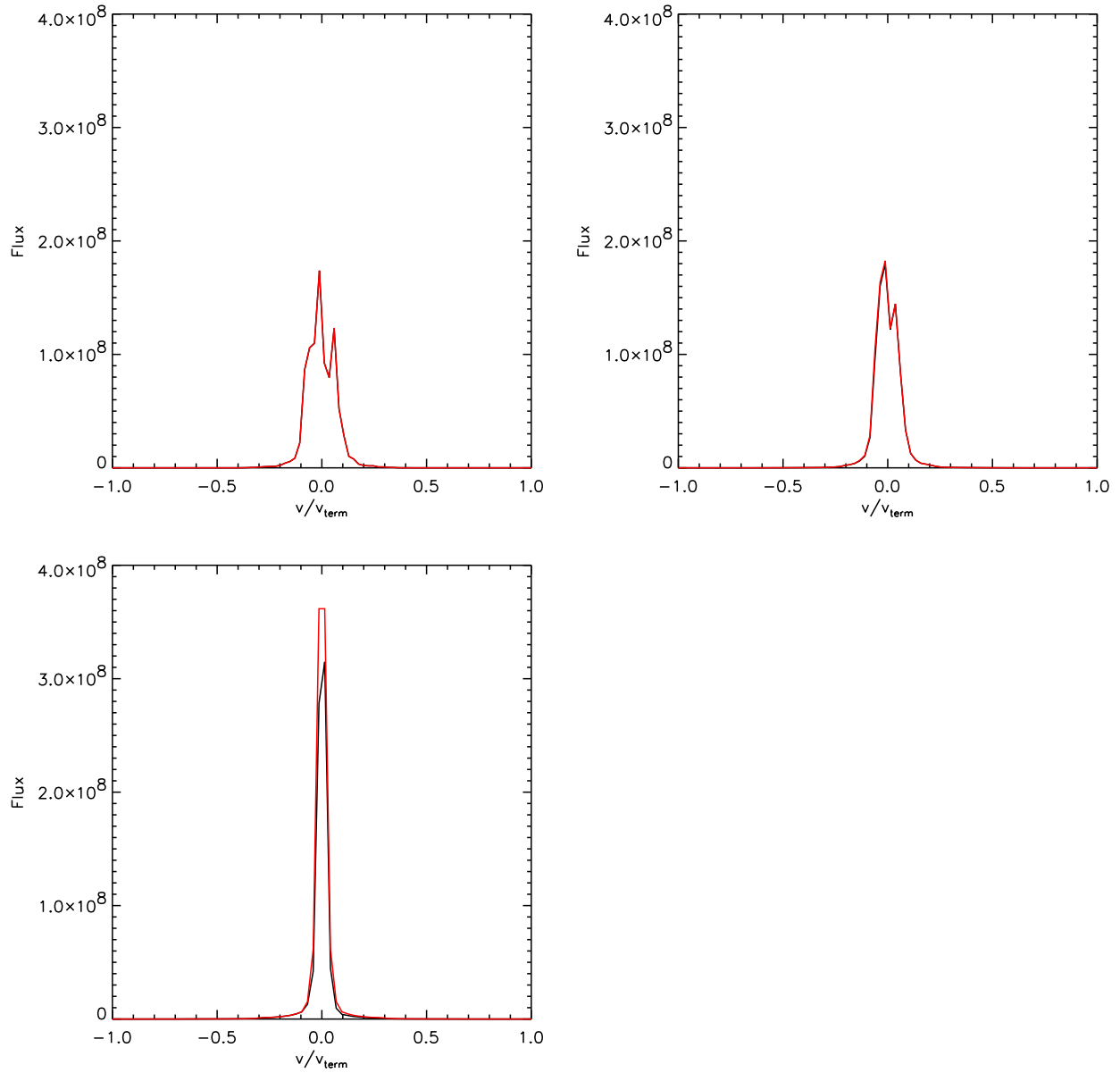


Fig. 19.— Above are the three line profiles from the 75 ks time in the MHD simulation. The red line is the unocculted wind, and the black line includes occultation. Again, the terminal velocity has been chosen to match the velocity stated in Donati et al (2002) of 2500 km/s. Clockwise from the top left is the polar view, the mid-view, and the equatorial view.

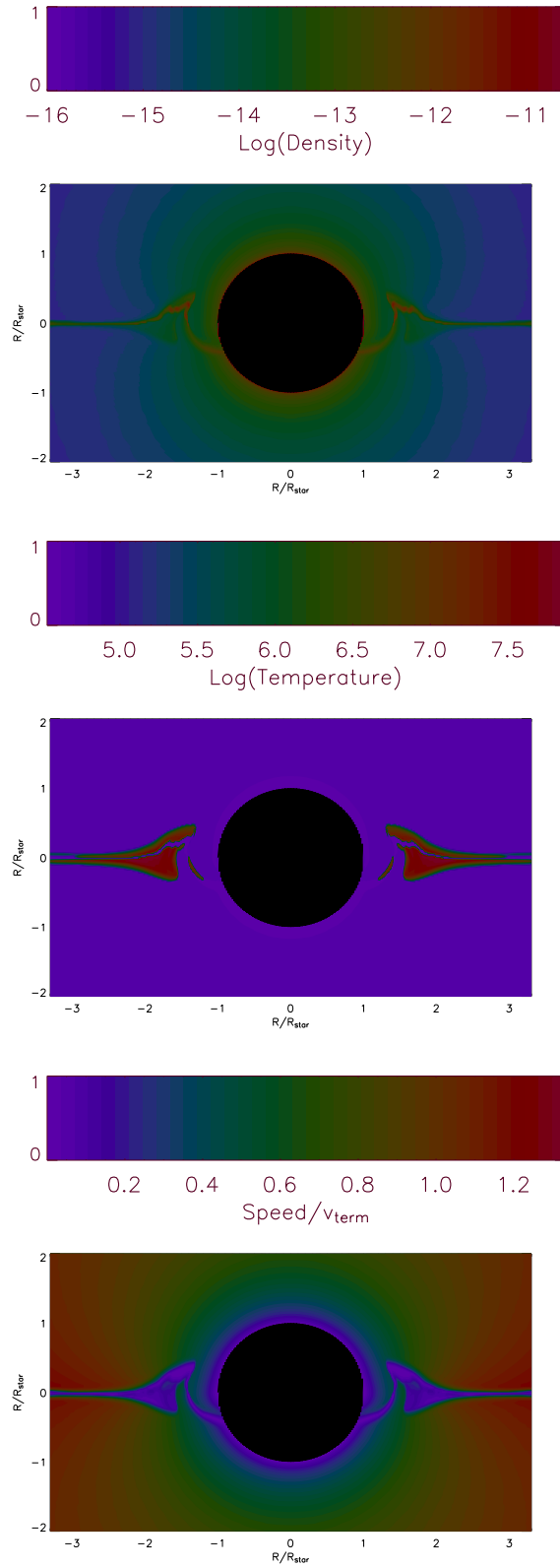


Fig. 20.— Above are three contour plots for an asymmetric time in the MHD simulation. (top) is the density contour plot, (middle) is the temperature contour, and (bottom) is the contour of speed. Note that the high density snake corresponds spatially to the low temperature snake.

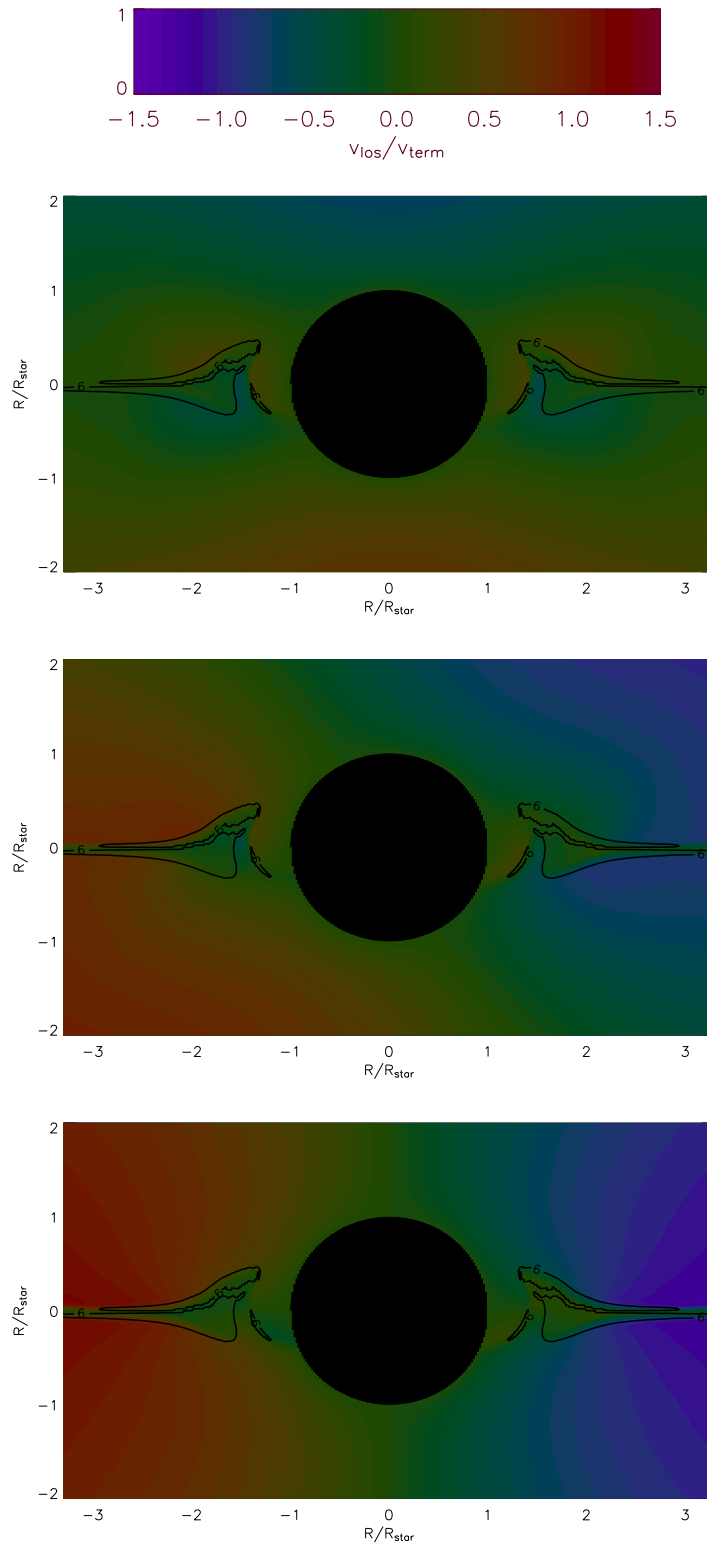


Fig. 21.— Above are the three contour plots from the line of sight velocity. The terminal velocity has been chosen to match the velocity stated in Donati et al (2002) of 2500 km/s. (top) Is the polar view, (middle) the mid-view, and (bottom) the equatorial view.

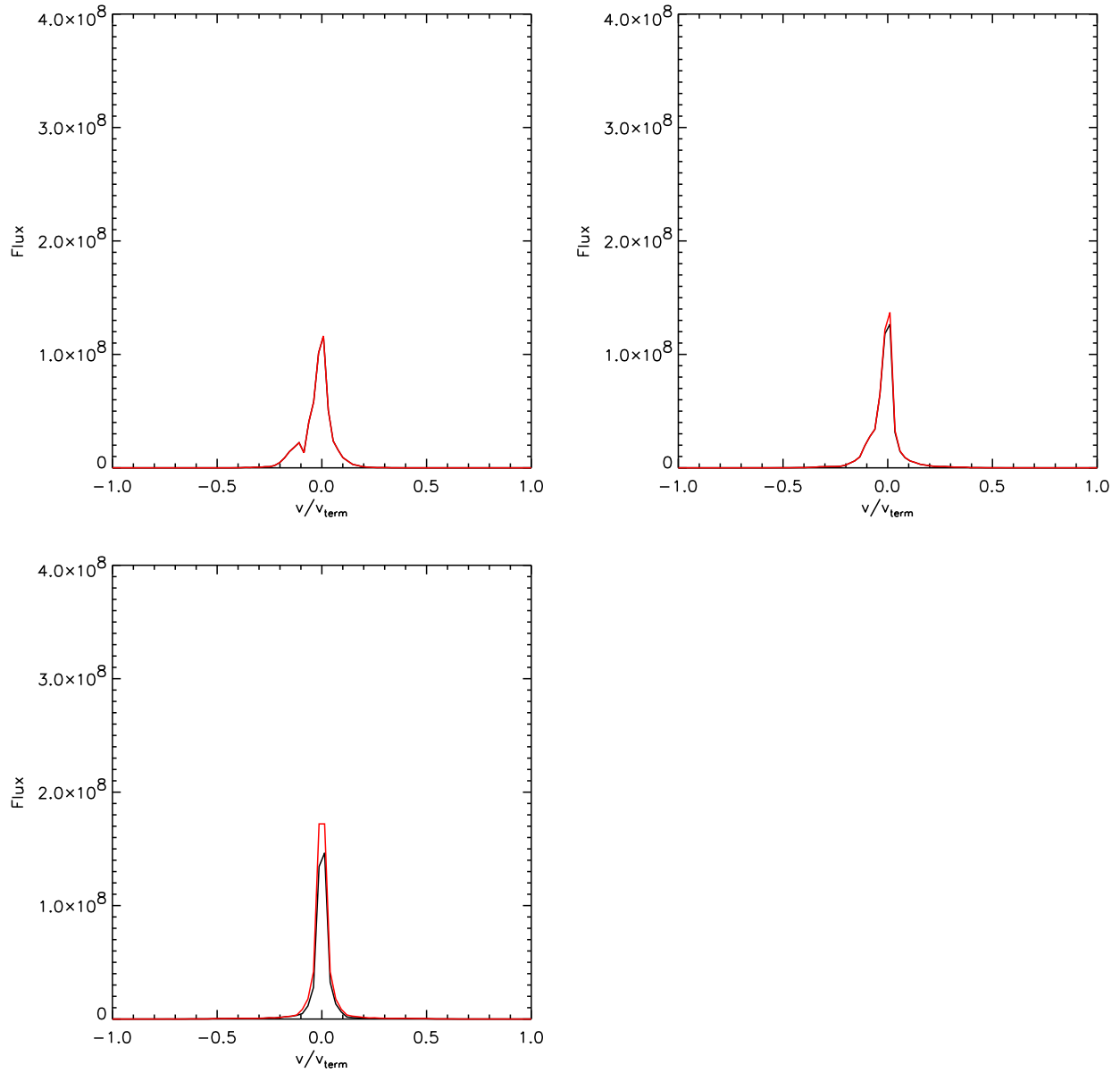


Fig. 22.— Above are the three line profiles from the 175 ks time. The red line is the unocculted wind, and the black line includes occultation. Again, the terminal velocity has been chosen to match the velocity stated in Donati et al (2002) of 2500 km/s. Clockwise from the upper left is the polar view, the mid-view, and the equatorial view.

To better understand our profiles, we created contour plots of density, temperature, and wind speed around the star (see Figure 17). This set of contours is from a time step in the MHD simulation at which the material has shocked at the equator and a dense disk has begun to form, at 75 ks. We note that the shocked wind is moving slowly, and that pre-shocked wind is moving up or down with respect to the magnetic pole along the field lines.

In conjunction with these general contours, we have made contours for this same time (75 ks) showing the line of sight velocities towards a viewer observing at three different viewing angles (Figure 18). There is a single contour outline at the 10^6 K emission boundary so we can focus only on the wind velocity within that temperature range.

Each of the line of sight contours has a corresponding line profile, as shown in Figure 19. First, we note that the widths of the lines do not expand with viewing angle. This is different from our analytic and isothermal models. In fact, the lines become thinner as viewing angle increases, although all the lines are narrow enough that width depends little on viewing angle. We also notice that the occulted wind is slightly blue-shifted. Although this must be because of the directionality of the occulted wind, before we make any conclusions regarding whether this is from turbulence or a real effect from the dipole flow of the wind we need to examine the wind velocities in more detail.

The contours and line profiles, however, change with time in the MHD simulation because there is no steady state solution. At other times, in particular at 175 ks, the dense material at the equator has become massive enough to be dragged back onto the star by gravity. We see in Figure 20 that these contours differ only with respect to the dense cool "snake" of material falling back onto the star. Although this cool material changes the contour plots drastically, it has little effect on the line profiles because it is too cool to emit X-rays and we do not consider attenuation by cool wind. The profiles in Figure 22, from 175 ks, show the same trend in width as the profiles in Figure 19, from 75 ks. The main difference between these two times is in the amount of flux. This can be explained by considering the two line of sight figures. In the 175 ks contour plot (Figure 21), less material seems to be within the 10^6 K temperature contour than in the 75 ks contour plot (Figure 18). The similarity in the line profiles from the 75 ks time and the 175 ks time leads us to believe that implementing the "soccer-ball" method (Dessart & Owocki, 2002) will not drastically change our profiles.

5. Comparisons with Data

5.1. θ^1 Orionis C

θ^1 Orionis C is a zero-age main sequence star with an age of about 200 000 yr (Donati et al., 2002), which is very young. It is an O star, with a temperature of about 45000 +/- 1000 K (Howarth and Prinja, 1989). By examining the period of the variability in the spectral lines, it has been determined that the rotational period of the star is 15.4 d. This is a very long period for an O-star, as they are normally rapid rotators. The mass-loss rate estimated by Howarth and Prinja is $4 \times 10^{-7} M_{\odot} \text{ yr}^{-1}$. Stahl et al. (1996) derive a wind terminal velocity larger than 2500 km s^{-1} , which is twice the escape velocity. By assuming a dipole structured magnetic field, Donati et al. (2002) modeled spectropolarimetric data and solved for a strong (1100 Gauss) field on θ^1 Orionis C. Donati et al. (2002) uses an angle of 42 ± 6 degrees for the angles between the rotational and magnetic axes. They also derive an angle of 45 degrees between the observer and rotational axis based on the difference between the period and the line of sight rotational velocity estimate of Stahl et al. (1996).

$$v_{los} = v \sin i \quad (17)$$

As shown in Figure 3, this allows observers a rare opportunity to study the star from all possible angles with respect to the magnetic axis.

5.2. Data

We have observed θ^1 Orionis C with the *Chandra* satellite. *Chandra* has heretofore unprecedented resolution. The High-Energy Transmission Grating Spectrometer (HETGS) allows for high-resolution spectroscopy between 1.2 and 31 Angstroms with a peak spectral resolution ³ of

$$\frac{\lambda}{\Delta\lambda} \simeq 1000 \quad (18)$$

Using the Doppler equation, this corresponds to 300 km s^{-1} .

We have data for four observation angles, as shown in Figure 3. We see numerous emission lines and a moderately strong continuum. At all of the viewing angles, the emission lines are narrow and symmetric. The line profiles have centroid shifts consistent with zero velocity. We have not found any statistically significant changes in the widths or shapes of

³(<http://cxc.harvard.edu/proposer/POG/html/HETG.html#chap:hetg>)

the line profiles of any line observed. In the following subsection, we compare our simulation results to the properties of roughly eight strong, unblended lines.⁴

5.3. Comparison

In this section we discuss comparisons of our theoretical models and the observational data of θ^1 Orionis C. We have performed three quantitative comparisons between our theoretical line profiles and actual data. We find that our MHD simulations produce emission lines that are consistent with the data when compared using three specific criteria: light curves, line centroid shifts, and line widths. When comparing the line widths of profiles created using our analytic models to the observed lines, we find that the analytic models produce broad lines that do not fit the data. The terminal velocity of θ^1 Orionis C has been calculated at 2500 km s^{-1} . The observed line profiles have full width half maximum (FWHM) values of no more than 300 km s^{-1} , less than twelve percent of the terminal velocity. Our analytic models consistently have FWHMs of over thirty percent of the terminal velocity. Thus, our analytic models cannot fulfill one of our main objectives, to reproduce the narrowness of the observed lines. We use these models as diagnostics rather than as possible θ^1 Orionis C wind structures. We note, however, that the analytic models successfully created symmetric line profiles, which was another objective of our research.

We have compared normalized light curves of the observational data and the post-processed MHD simulation, as shown in Figure 23. Our modeled light curve includes the flux at all the relative velocities from 75 ks versus the viewing angle. The simulated curve is a good initial match to the data. Not only does the flux decrease with viewing angle in both the data and the model, it also decreases by a similar percentage in each. As the viewing angles increases, more of the equatorial wind is occulted by the star and more of the flux is blocked. Because we see this effect in both the model and the data, our model’s geometry, with the emitting wind near the equator, is likely the same as the geometry of θ^1 Orionis C. Based on this information we are able to map the locations of the emitting zones in the wind with respect to the magnetic field. Because the observed reduction in flux must be due to occultation by the star, the emitting wind is concentrated around the magnetic equator.

We can show that occultation by the star is the reducing mechanism, instead of absorption by the cooling disk, by comparing the light curves of two of our analytic models to the data. The two models we compare are the equatorial flared disk model and the dipole model. The flared disk model has a light curve that depends only on occultation, while the

⁴The data reduction was performed by M. Oksala & M. Gagne

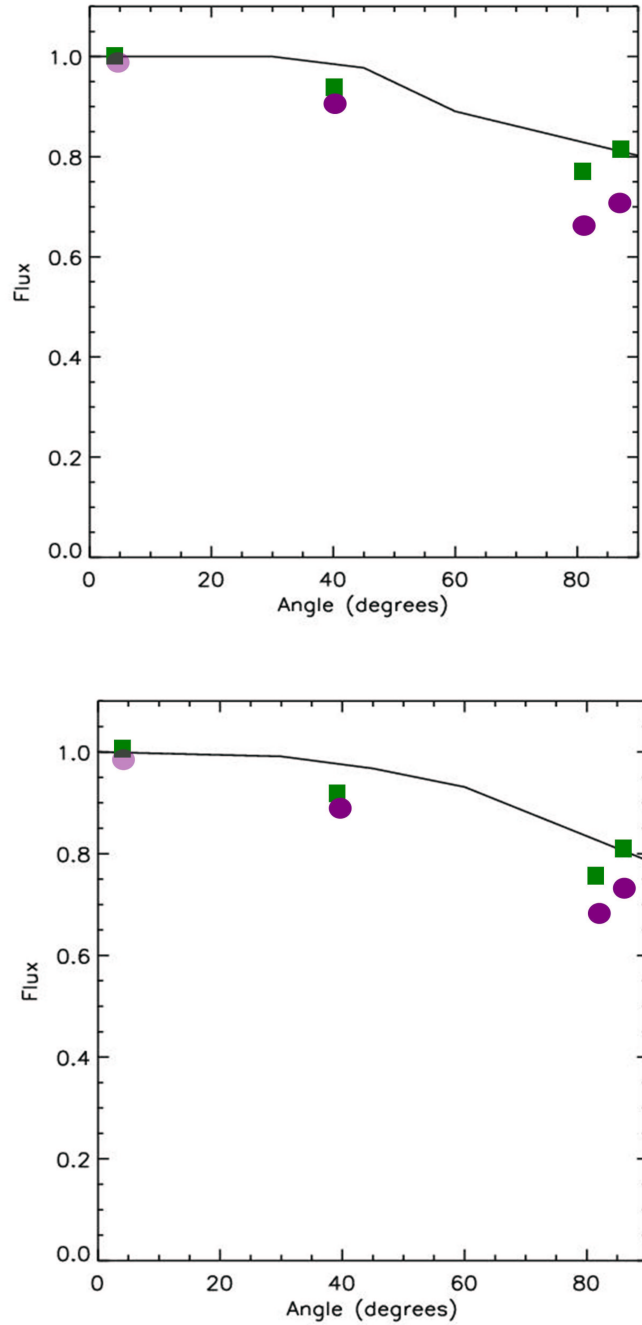


Fig. 23.— The lightcurves shown above are for two different times in the MHD simulation. The first is from a time at which the equatorial disk is formed, and the second when there is a snake of dense material falling back onto the star. The shapes on the diagram are normalized flux levels from the data. The purple circles are from lower energy lines of between 10-15 Å. The green are from lines with about a 5 Å wavelength.

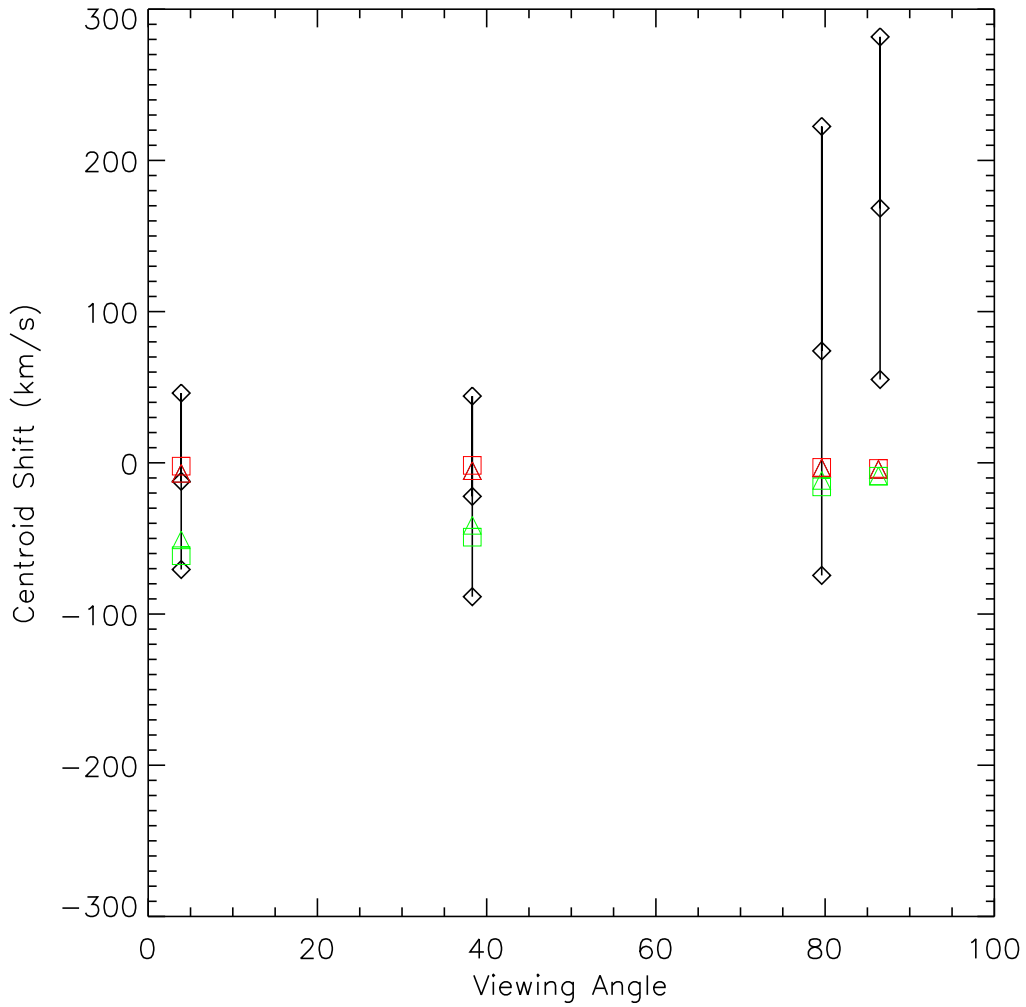


Fig. 24.— This plot shows the shift of the centroids from zero velocity of both observed and modeled lines. The black diamonds mark the median shift with error bars of the shifts from all the lines observed at that viewing angle. The red objects mark shifts from the 75 ks simulation, the green from 175 ks. The triangles are shifts of lines that are emitted above 10^6 K and the squares mark lines that are emitted above 10^7 K.

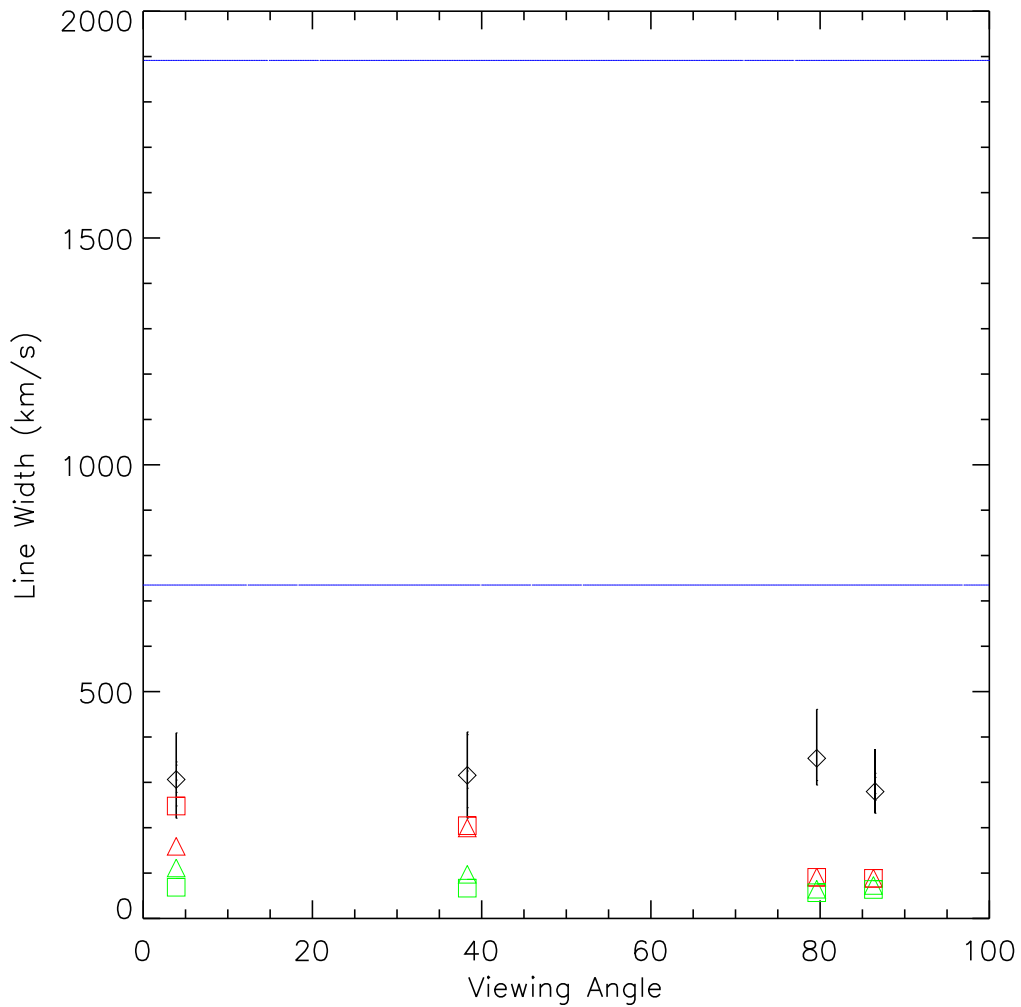


Fig. 25.— This plot shows the linewidths of both observed and modeled lines. The lines range from the minimum observed turbulent velocity at that angle, and the diamonds mark the mean turbulent velocity. The points from the simulation have the same demarcating scheme as in the previous figure. The two blue lines delimit the range of turbulent velocity for another O star, ζ Puppis, that is a standard wind shock source.

dipole model’s light curve depends on both occultation and attenuation by a cooling disk at the equator. Although the dipole model has an unrealistically opaque cooling disk, its light curve remains informative. In direct contrast to the trends seen in the equatorial disk model (Figure 12) and the data, the dipole model’s flux increases with viewing angle (Figure 15). Thus we verify that occultation has a larger effect on the total flux than absorption by a cooling disk.

We have also examined the centroids of the observed and simulated lines. The data range from having centroids at -100 km s^{-1} to 300 km s^{-1} . We calculate the centroid of a modeled line using an integral.

$$\bar{v} = \frac{\int vF(v)dv}{\int F(v)dv} \quad (19)$$

,where $F(v)$ is the flux at some velocity. In our program we approximate these integrals using summation over all discrete values of velocity and emission. The centroids of the modeled lines are all consistent with zero velocity, whether the lines are from the stable time, 75 ks, or the unstable time, 175 ks. The emission threshold, whether 10^6 K or 10^7 K , also has no effect on the centroid shift (Figure 24). In our models, the centroid shift is always smaller in the lines from the 75 ks time than in the lines from the 175 ks time. This may be because 75 ks is the more stable time, with no material falling back onto the star. The emitting temperature threshold, whether 10^6 K or 10^7 K , does not affect the centroid shift significantly. All of our calculated centroids are consistent with zero shift, and thus consistent with the data from $\theta^1 \text{ Orionis C}$.

Finally, we have examined the turbulent velocity, also called the b parameter. This is related to the full width half maximum of an emission line by $FWHM = 1.66b$. The corresponding value for the data is the turbulent velocity. The equation used to find this value is an equation solving for the Doppler width of the lines (refer to equation 3):

$$\begin{aligned} \Delta\lambda &= \frac{\lambda_o}{c} \left(\frac{2kT}{m} + \zeta^2 \right)^{0.5} \\ \Delta\lambda &= \frac{FWHM}{1.665} \end{aligned} \quad (20)$$

where λ_o is the rest wavelength, and the total velocity is the thermal velocity and the turbulent velocity added in quadrature with ζ as the turbulent velocity. Although our b parameter is not exactly equal to $\Delta\lambda$ because it does not include thermal broadening, we can ignore the thermal broadening of the line because it is so much smaller than the turbulent velocity. When the two are added in quadrature, the thermal velocity has little effect on the total velocity. We do not attempt to model the thermal velocity because we are not considering specific ions in our general model.

We found that our b parameter, as calculated from the FWHM of lines created by the MHD simulation, is almost always smaller than the turbulent velocity of the data. The difference is smallest in the 75 ks time with an emission threshold temperature of 10^7 K. Although we find that our calculated values of turbulent velocity are not a perfect match to the θ^1 Orionis C data, they are much closer to these turbulent velocities than to the turbulent velocities of other O stars, such as ζ Puppis. This is easily seen by examining Figure 25. The ζ Puppis lines have a turbulent velocity of about 1200 km s^{-1} (Cassinelli et al., 2001), while the maximum turbulent velocity of any of the observed lines of θ^1 Orionis C is below 300 km s^{-1} . Our theoretical lines have turbulent velocities between 55 km s^{-1} and 250 km s^{-1} , with the lowest velocities at the unstable 175 ks time.

One way in which our theoretical turbulent velocities do match our observations is that they remain constant across the range of viewing angles. Our model’s success in predicting this consistency is another piece of evidence that θ^1 Orionis C has a magnetically channeled wind. In this section we have examined several correlations between the theory and the data. The narrowness and symmetry of the observed emission lines are two properties that we hoped to reproduce using our adapted MCWS model. We were successful in this; we also found that the centroid shifts are similar in the lines from both data and the simulation.

6. Conclusions

Our adaptation of the MCWS model can potentially explain the narrow and symmetric lines seen in four of the five stars in the Orionis trapezium (Schulz, 2002), especially θ^1 Orionis C. The emission lines generated by the latest MHD simulations have narrow line widths and centroids that are consistent with our observed lines from θ^1 Orionis C. Therefore, we conclude that the wind structure on θ^1 Orionis C closely matches that of our magnetically channeled wind model.

We created analytic models that we used as diagnostic tools to determine where the emitting wind is located and whether absorption has a large effect on the line profiles. We also used custom-calculated MHD simulations to create the most realistic models of a magnetically channeled wind. Our success in fitting both line profiles and light curves is unprecedented.

These are the first line profiles ever calculated from a numerical simulation. In creating our line profiles, we considered only three factors: Doppler broadening, occultation, and viewing angle. Our calculated Doppler shifts of the emitting material only broaden the line profiles slightly, producing the desired narrow emission lines. The dependence of the

occulted wind material on the viewing angle is evidenced by our lightcurves, which mimic the real data using only occultation to determine the amount of flux seen at each observing angle. We briefly considered absorption by a cooling equatorial disk in the analytic dipole model. However, when we examine the light curves from our dipole model (Figure 15) and our equatorial flared disk model (Figure 12) we find that the light curve resulting from only occultation matches the light curve of the data (Figure 23) better than the light curve resulting from the cool equatorial disk. This result speaks directly to our interpretation of the wind geometry. The light curve of θ^1 Orionis C shows that the cooling disk, if present, does not have a strong attenuating effect.

We also do not consider the possible effects of rotation. Although it may be that in some hot stars the velocity profile of the magnetically channeled winds will be highly dependent on the azimuthal velocity, in the specific case of θ^1 Orionis C we reason that the rotation period is slow, so the overall effect on the velocity of the wind will be minimal. In addition, the forty-five degree angle between the observer’s axis and the rotation axis will cause the azimuthal velocity that we observe to be a factor of $\sqrt{2}$ less than the actual rotational velocity. In order to make our model applicable to all O stars with magnetic fields, we may need to add azimuthal velocity to our wind.

With our production of line profiles created by using different threshold emission temperatures, we have taken the first step towards creating line profiles that correspond to specific ions. We may continue this in the future with the boundaries of our emission temperature ranges defined by ion transitions.

Another addition to our model will be to introduce azimuthal variation. Currently we use the output from the two dimensional MHD simulation, and assign the same velocity, temperature, and density profile to every azimuthal slice. This means that if there is a cooling disk at one particular ϕ value, this exact cooling disk occurs at every azimuthal angle. Figures 17 and 20 display the differences over time of the two dimensional MHD simulation. There is a high probability that these fluctuations of the cooling disk do not have the same time dependence throughout the disk because of their random nature. Thus, during any one observation of a star with a magnetically channeled wind there will be a range of two dimensional velocity, density and temperature profiles at different azimuthal angles around the star.

Our final foreseen addition is to add absorption from cooler parts of the wind. This should verify the claim that absorption of X-rays by cooler material is minimal (Waldron & Cassinelli, 2001). This is not a trivial calculation, because it involves interpolating our spherical grid into a cylindrical grid whose z -axis is parallel to the observer’s line of sight. We will then multiply the emission from each zone by the attenuation (equation 16) from

the nearest zone of cool wind in the line of sight towards the observer. The emission that exits the cool zone will then be attenuated by the next cool zone along the line of sight to the observer. This will continue until the light exits the wind.

Even without these additions, our model is sophisticated enough to fit the data from θ^1 Orionis C. The adapted MCWS model is the best solution to the problem of why some O stars have narrow, symmetric X-ray lines because it matches the data using only known physical phenomena.

I would like to gratefully acknowledge my diligent editors. I would also like to thank my supportive family and friends. Finally, without my advisor this would not have been possible.

REFERENCES

- Baade, D. & Lucy, L. B. 1987, *A&A*, 178, 213
- Babel, J., & Montmerle, T. 1997, *ApJ*, 485, L29
- Cassinelli, J. P., Miller, N. A., Waldron, W. L., MacFarlane, J. J., & Cohen, D. H. 2001, *ApJ*, 554, L55
- Cassinelli, J. P., & Olson, G. L. 1979, *ApJ*, 229, 304
- Cassinelli, J. P., Olson, G. L., & Stalio, R. 1978, *ApJ*, 220, 573
- Cassinelli, J. P. & Swank, J. H. 1983, *ApJ*, 271, 681
- Dessart, L. & Owocki, S. P. 2002, *A&A*, 383, 1113
- Donati, J.-F., Babel, J., Harries, T. J., Howarth, I. D., Petit, P., & Semel, M. 2002, *MNRAS*, 333, 55
- Gagne, M., Caillault, J., Stauffer, J. R., & Linsky, J. L. 1997, *ApJ*, 478, L87
- Harnden, F. R. et al. 1979, *ApJ*, 234, L51
- Hillier, D. J., Kudritzki R. P., Pauldrach, A. W., Baade, D., Cassinelli, J. P., Puls, J., & Schmitt, J. H. M. M. 1993, *A&A*, 276, 117
- Howarth, I. D. & Prinja, R. K. 1989, *ApJS*, 69, 527
- Kramer, R. H., Cohen, D. H., & Owocki, S. P. submitted 2003, *ApJ*

- Lamers, H. J. G. L. M., & Cassinelli, J. P. 1999, *Introduction to Stellar Winds* (Cambridge: Cambridge University Press)
- Macfarlane, J. J., Waldron, W. L., Corcoran, M. F., Wolff, M. J., Wang, P., & Cassinelli, J. P. 1993, *ApJ*, 419, 813
- Nordsieck, K. H., Cassinelli, J. P., & Anderson, C. M. 1981, *ApJ*, 248, 678
- Ostlie, D. A., & Carroll, B. W. 1996, *An Introduction to Modern Stellar Astrophysics* (Reading: Addison-Wesley Publishing Company, Inc.)
- Owocki, S. P., Castor, J. I., & Rybicki, G. B. 1988, *ApJ*, 335, 914
- Schulz, N. S., Canizares, C. R., Huenemoerder, D., & Lee, J. C. 2000, *ApJ*, 545, L135
- Schulz, N. S., Huenemoerder, D., Canizares, C. R., & Tibetts, K. 2002, *American Astronomical Society Meeting*, 201,
- Seward, F. D., Forman, W. R., Giacconi, R., Griffiths, R. E., Harnden, F. R., Jones, C., & Pye, J. P. 1979, *ApJ*, 234, L55
- Stahl, O. et al. 1996, *A&A*, 312, 539
- ud-Doula, A., & Owocki, S. P. 2002, *ApJ*, 576, 413
- Waldron, W. L., & Cassinelli, J. P. 2001, *ApJ*, 548, L45